Direct visualization of emergent metastatic features within an *ex vivo* model of the tumor microenvironment

Libi Anandi[§], Jeremy Garcia[§], Manon Ros, Libuše Janská, Josephine Liu, Carlos Carmona-Fontaine*

Center for Genomics & Systems Biology, Department of Biology, New York University, New York, NY 10003, USA

[§]These authors contributed equally to this work

*Correspondence: cf97@nyu.edu

ABSTRACT

Metabolic conditions such as hypoxia, nutrient starvation, and media acidification, together with interactions with stromal cells are critical drivers of metastasis. Since these conditions arise deep within tumor tissues with poor access to the bloodstream, the observation of nascent metastases *in vivo* is exceedingly challenging. On the other hand, conventional cell culture studies cannot capture the complex nature of metastatic processes. We thus designed and implemented an *ex vivo* model of the tumor microenvironment to study the emergence of metastatic features in tumor cells in their native 3-dimensional (3D) context. In this system, named 3MIC, tumor cells spontaneously create ischemic-like conditions, and it allows the direct visualization of tumor-stroma interactions with high spatial and temporal resolution. We studied how 3D tumor spheroids evolve in the 3MIC when cultured under different metabolic environments and in the presence or absence of stromal cells. Consistent with previous experimental and clinical data, we show that ischemic environments increase cell migration and invasion. Importantly, the 3MIC allowed us to directly observe the emergence of these pro-metastatic features with single-cell resolution allowing us to track how changes in tumor motility were modulated by macrophages and endothelial cells. With these tools, we determined that the acidification of the extracellular media was more important than hypoxia in the induction of pro-metastatic tumor features. We also illustrate how the 3MIC can be used to test the effects of anti-metastatic drugs on cells experiencing different metabolic conditions. Overall, the 3MIC allows us to directly observe the emergence of metastatic tumor features in a physiologically relevant model of the tumor microenvironment. This simple and cost-effective system can dissect the complexity of the tumor microenvironment to test perturbations that may prevent tumors from becoming metastatic.

INTRODUCTION

Most cancer fatalities are directly or indirectly caused by metastases[1]. Thus, treating pre-metastatic tumor cells before they acquire migratory and invasive properties could dramatically reduce cancer mortality[2]. Recent studies using *in vivo* mouse models have provided novel insights into the metastatic process such as the role played by DNA damage through the promotion of the cGAS-STING pathway[3], the increased metastatic efficiency of cell groups over single cells[4], key roles of stromal and immune cells[5–7], and conditions that facilitate the reactivation of dormant metastases and their engraftment into new tissues[8].

The direct observation of nascent metastases remains elusive. Unfortunately, the observation of metastases *in vivo* requires sophisticated microscopy with costs that are prohibitively expensive for most laboratories[9–11]. Tools including quantification of circulating tumor cells, histological analyses of biopsies, and warm autopsies[12–18] provide important information about late metastatic steps. However, early metastases are much more challenging to detect and to study[19–21]. This challenge is due in part to the complexity of cellular and molecular factors that regulate the emergence of metastasis [22–25]. In addition, the initiation of metastasis is a stochastic process and thus when and where a metastatic clone emerges is unpredictable[26–28]. Amid these limitations, we sought to model the initial conditions that favor the emergence of metastasis *ex vivo*.

A model of a premetastatic tumor must recreate microenvironmental factors that are critical in the regulation of metastasis such as altered metabolic conditions[22–25], and interactions with immune and stromal cells[22,29]. For example, in vivo imaging, molecular, and histological evidence have demonstrated and active role for tumor-infiltrated macrophages[5,30–32] and fibroblasts[33–36] in promoting and facilitating cancer invasion and metastasis. Metabolic stress in the tumor microenvironment is also associated with metastasis promotion[37–44]. Hypoxia is a common feature of solid tumors, and its pro-metastatic roles are well-established[40,41,45]. However, hypoxia rarely – if ever – occurs alone: as nutrients and oxygen diffuse into the tumor mass, oxygen and nutrients in the microenvironment become progressively scarcer while metabolic by-products, such as lactic acid, accumulate[46–53]. Most likely, multiple conditions

52 within an ischemic microenvironment, including redox stress[54], acidosis[43,55], nutrient starvation[56]
53 rather than hypoxia alone, drive the initiation of metastasis.

54 By definition, ischemic conditions usually arise deep within tumors, and thus accessing and
55 observing emergent metastases *in vivo* has been virtually impossible. Some aspects of tumor
56 biology are well captured by *ex vivo* cultures such as organoids[57–64] and other 3D tumor model
57 systems[65–68]. Still, in these models, ischemic tumor cells remain buried within these structures
58 and thus imaging tumor-stromal interactions in those regions poses an almost insurmountable
59 challenge.

60 Here we present the development of an *ex vivo* model of the tumor microenvironment designed
61 to visualize the transition of poorly motile primary tumor cells into migratory metastatic-like cells.
62 This 3D Microenvironmental Chamber or 3MIC, models key tumor features including the
63 infiltration of immune cells and the spontaneous formation of metabolic gradients that mimic the
64 metabolic conditions within tumors. Due to its unique geometry, the 3MIC easily allows imaging
65 ischemic cells with unprecedented temporal and spatial resolution. Using this system, we show
66 that ischemic-like environments directly drive the emergence of metastatic features including
67 increased cell migration, degradation of the extracellular matrix (ECM), and loss of epithelial
68 features. Combining *in vivo* experiments with 3MIC cultures, we showed that these changes
69 were reversible suggesting that metastatic features can arise even in the absence of clonal
70 selection by hypoxia or other environmental challenges. We also show that tumor interactions
71 with stromal cells such as macrophages and endothelial cells, increase the pro-metastatic
72 effects of ischemia. Finally, we illustrate how the 3MIC can be used to test how local metabolic
73 conditions may affect drug responses. In all, the 3MIC is an affordable cell culture system where
74 different components of the tumor microenvironment can be carefully dissected. Its amenability
75 for live imaging can complement *in vivo* studies to better understand and treat the emergence of
76 metastases.

77 **RESULTS**

78 **A 3D *ex vivo* model of the tumor microenvironment for the direct visualization of**
79 **ischemic cells**

80 Insufficient vascularization and excessive cell growth leave large ischemic regions within solid
81 tumors[46–53]. Hypoxia, acidosis, and other metabolic stressors associated with ischemia, are
82 known drivers of metastasis. Since these metabolic conditions often arise deep within tumors,
83 visualizing the emergence of metastatic properties *in vivo* or in 3D organoids, presents unique
84 technical challenges (Fig. 1A). To overcome these limitations, we first thought to use the
85 **Me**tabolic **Mi**croenvironment **C**hamber (MEMIC), an *ex vivo* model of the tumor
86 microenvironment that we developed to study the impact of ischemic stress on cell cultures[69–71].
87 In this system, cell monolayers form reproducible gradients of ischemia and by design imaging
88 ischemic cells is as easy to as imaging well-nurtured cells.

89 Key features of metastatic cells involve morphological changes that are better modeled by 3D
90 tumor structures than by cell monolayers. The MEMIC was designed for 2D cultures, and the
91 density of these cells is crucial for the formation of metabolic gradients[71]. Unfortunately, this
92 system did not allow achieving enough cell density in 3D cultures to form detectable ischemic
93 gradients (Fig. S1A). We thus designed and developed a new system – which we named **3**D
94 **mi**croenvironment **c**hamber (3MIC) – to study the impacts of the metabolic microenvironment
95 on 3D cultures. The principle behind the 3MIC is similar to the one of the MEMIC: we grow a
96 dense monolayer of cells inside a small chamber that is restricted from accessing nutrients and
97 oxygen from all sides but one. The opening on this side connects to a large volume of fresh
98 media and thus it acts as a source of nutrients and oxygen, while cells inside the chamber act
99 as resource sinks. In the 3MIC, however, these cells are not the focus of our analyses and only
100 act as nutrient consumers. These “consumer cells” grow upside-down on a coverslip at the top
101 of the chamber and underneath them, we can introduce 3D tumor structures embedded in ECM.
102 This two-tier system should allow us to have a high-density consumer cell layer producing
103 strong metabolic gradients within a microenvironment shared by much sparser 3D tumor
104 structures that in turn have a negligible impact on the metabolic conditions of the chamber (Fig.
105 1B; Fig. S1B). The location of consumer cells on top of the chamber allows an unobstructed

106 view of the 3D tumor structures which will be closer to the objective of an inverted microscope
107 (Fig. 1B). These experiments can use different combinations of cell types to form spheroids and
108 the consumer layer. For simplicity, however, and unless mentioned otherwise, experiments
109 shown here use the same cell type for both roles.

110 To test the 3MIC, we first confirmed that consumer cells form metabolic gradients. As a proxy
111 for resource deprivation, we used a fluorescent hypoxia sensor (HRE-GFP[71]) which we
112 expressed in a panel of epithelial tumor cells co-expressing constitutive plasma membrane
113 fluorescence (mCherry-CAAX[71]). As in our MEMIC experiments, 2D monolayers of consumer
114 cells formed strong ischemic gradients. For example, spheroids formed by Lung KP cells
115 (derived from a murine model of lung adenocarcinoma driven by $KRAS^{G12D}$ and loss of TP53[72])
116 cells displayed a strong gradient of GFP that increased with the distance to the opening of the
117 3MIC (Fig. S1C). We then aggregated cells into small tumor spheroids that we embedded in a
118 collagen- and laminin-rich ECM scaffold and introduced them into 3MICs with or without
119 monolayers of consumer cells.

120 As expected, spheroids in control 3MICs without consumer cells did not show signs of hypoxia
121 (Fig. 1C,D). In contrast, tumor spheroids growing in 3MICs under consumer cells showed levels
122 of the GFP hypoxia reporter that increased with the distance to the opening of the chamber (Fig.
123 1C,D). We obtained similar results with three independently derived clones of Lung KP cells and
124 in experiments using different cell lines, and in different cell types expressing a different hypoxia
125 reporter[73] (Fig. S1D). These results show that consumer cells in the 3MIC form metabolic
126 gradients that influence the local metabolic microenvironment of neighboring tumor spheroids.
127 As these metabolic gradients in the 3MIC are perpendicular to our imaging path, we can
128 observe how ischemic conditions affect tumor structures with unprecedented spatial and
129 temporal resolution.

130 **Hypoxia is required but not sufficient to increase invasive features in tumor spheroids**

131 In these experiments we observed that the morphology of tumor spheroids changed
132 dramatically along the 3MIC. Ischemic spheroids acquired a ruffled and protrusive morphology
133 suggesting an increased invasive behavior (Fig. 2A; Video S1). In contrast, well-nurtured
134 spheroids close to the opening had a modest size increase and remained mostly smooth and

135 rounded (Fig. 2A; Video S1). We decided to take advantage of the unique features of the 3MIC
136 to identify the specific conditions that trigger these seemingly pro-metastatic features on
137 ischemic spheroids.

138 There is ample evidence linking hypoxia to pro-metastatic tumor features[37–44]. However,
139 whether additional metabolic stressors – such as nutrient deprivation or lactic acid accumulation
140 – may contribute to the morphological changes we observe in the 3MIC. To rapidly compare the
141 effects of different treatments on spheroid morphology, we defined *invasiveness index* as the
142 inverse of their circularity. This index increases in cellular structures with irregular and protrusive
143 shapes and remains small in smooth and homogeneous tumor spheroids (Fig. 2B).

144 We first tested whether hypoxia was sufficient to trigger morphological changes and increase
145 cell migration in tumor spheroids. We compared spheroids cultured in regular petri dishes
146 incubated under different oxygen tensions (21% and 1%) with spheroids cultured in the 3MIC.
147 Tumor spheroids cultured in a hypoxic incubator increased levels of the GFP-based hypoxia
148 sensor to levels comparable to ischemic clusters in the 3MIC (Fig. S2A). Hypoxic spheroids,
149 however, were not as invasive as spheroids in the 3MIC and were only slightly more invasive
150 than spheroids cultured in regular incubators (Fig. 2C). In similar experiments, we treated
151 spheroids with dimethyloxalyglycine (DMOG) or cobalt chloride ($CoCl_2$) – two prolyl
152 hydroxylation inhibitors that stabilize the transcription factor Hypoxia-inducible factor 1-alpha
153 (HIF1A) and trigger a hypoxic-like transcriptional response under normal oxygen tension[74]. As
154 shown in Figure 2D, these spheroids showed only modest increases in invasion despite a
155 strong activation of HIF1A response, as denoted by the strong increase in the GFP signal from
156 the hypoxia reporter (Fig. 2D, Fig. S2B). These results show that hypoxia alone triggers
157 relatively minor morphological changes and cannot fully recapitulate the changes that we
158 observe in ischemic regions of the 3MIC.

159 Additional experiments however revealed that while not *sufficient*, hypoxia was *required* in
160 altering spheroid morphologies in ischemia. First, we took advantage of the selective
161 permeability of polydimethylsiloxane (PDMS)[69–71]. PDMS is permeable to oxygen and other
162 gases, but not to soluble metabolites[75]. We thus constructed 3MICs using a PDMS membrane
163 molded into the shape of a glass coverslip. In these modified 3MICs, cells form gradients of

164 nutrients and metabolic byproducts, but oxygen rapidly equilibrates across the PDMS
165 membrane and thus there is no hypoxia (Fig. S2C). Under these conditions, tumor spheroids did
166 not show major morphological challenges, regardless of whether consumer cells were present
167 or not (Fig. 2E; Fig. S2C). Second, we established that the changes displayed by ischemic
168 spheroids require HIF1A signaling. Using CRISPR/Cas-9 we generated isogenic knockout Lung
169 KP cells (Hif1a$^{-/-}$). As expected, Hif1a$^{-/-}$ cells did not have detectable levels of HIF1A-even after
170 treatment with DMOG (Fig. 2F) and did increase their hypoxia-driven GFP levels when cultured
171 in a hypoxic incubator (Fig. S2D). As in previous experiments, isogenic wildtype cells (Hif1a$^{+/+}$)
172 showed strong morphological changes along the 3MIC but these changes were severely
173 impaired in spheroids formed by Hif1a$^{-/-}$ cells (Fig. 2G). Altogether, these results show that
174 hypoxia and HIF1A signaling are required but not sufficient for the morphological changes seen
175 in ischemic clusters. As the effects of these perturbations alone are weak, we thought that cells
176 need additional metabolic cues to fully adopt the morphologies we observe in ischemic
177 spheroids.

178 **Media acidification is critical for the increase in metastatic features displayed by**
179 **ischemic tumor cells**

180 We then sought for additional factors that may increase the invasive capacity of tumor
181 spheroids. A simple look with the naked eye at a 3MICs culture would suggest that strong
182 changes in pH are occurring inside. We regularly use cell culture media with the pH indicator
183 phenol red which show its typical red color near the opening of the chamber gradually yellowing
184 deeper with the 3MIC (Fig. S2E). A ratiometric analysis of this change showed that extracellular
185 pH levels drastically decrease in ischemic regions while they remained relatively constant in
186 3MICs without consumer cells (Fig. 2H,I).

187 Changes in intracellular pH were much milder (Fig. S2F). We thus focused on factors affecting
188 media acidification such as lactic acid, which is abundantly produced and secreted by the
189 glycolytic metabolism of tumors. Surprisingly, the simple addition of lactic acid to tumor
190 spheroids under otherwise well-perfused and normal conditions, strongly increased their
191 invasiveness (Fig. 2J). Consistent with a key role of low pH in promoting cell invasion, addition
192 of bicarbonate to increase the buffering capacity of the media, eliminated the invasiveness of

193 ischemic spheroids in the 3MIC (Fig. 2K). Importantly, acidification of the extracellular
194 environment has been linked to increased tumor invasion and metastasis[43,76,77].

195 Together, these results show that HIF1A signaling is required to increase the invasion of
196 ischemic spheroids while a low pH is sufficient to do so. We speculate that these effects are
197 linked as HIF1A increases lactic acid secretion through its regulation of glycolysis[78]. We think
198 that in normal cultures, or in well-perfused tissues, lactic acid levels do not rise enough to
199 produce a strong pH decrease. But in the 3MIC or in poorly vascularized tissues such as solid
200 tumors, lactic acid is not cleared rapidly enough and thus it accumulates increasing cell invasion
201 through a pH reduction (Fig. 2L). These experiments illustrate the importance of considering
202 ischemia as a whole rather than hypoxia alone and they illustrate the ease of modeling these
203 complex metabolic microenvironments in the 3MIC.

204 **Ischemia stimulates persistent cell migration**

205 The increased invasion of ischemic spheroids was conserved across a panel of human and
206 mouse cell lines (Fig. S3A,B). To better understand the mechanisms behind these changes, we
207 first ruled out a major contribution for cell proliferation changes that can also drive the expansion
208 of cell populations[79,80]. In fact, only a small number of cells in our 3D cultures were actively
209 proliferating as revealed by a sparse signal for phospho-H3 immunostaining (Fig. S3C) and by
210 FUCCI-based live imaging of the cell cycle (Fig. S3D; Video S2).

211 In contrast, live imaging analyses showed a significantly higher cell dispersion in ischemic
212 clusters quantified as a decrease in local cell density (Fig. 3A,B; Video S3)[69]. Taking advantage
213 of the high temporal and spatial resolution in live microscopy afforded by the 3MIC, we
214 measured the migratory properties of individual tumor cells. Cells in these 3D structures are
215 tightly packed muddling cell detection and tracking. To avoid this problem, we formed chimeric
216 spheroids by mixing two populations of Lung KP cells expressing a nuclear fluorescent protein
217 (H2B-YFP) or mCherry-CAAX typically in a 1:10 ratio (Fig. 3C; Video S4). We can then easily
218 track H2B-YFP-positive as they are much sparser, and their nuclear label is easy to detect.
219 Using automated image analysis tools, we tracked hundreds of cells from different spheroids
220 along the gradient of ischemia. Analysis of nearly 900 tracks of individual cells showed a large
221 heterogeneity in their motility where some cells wandered near their origins, while others moved

222 over large distances. On average, however, cells from ischemic clusters traveled further from
223 their original location than cells from well-nurtured clusters (Fig. 3D, Fig. S3E,F; Video S4). This
224 increase in net displacement was not due to an increase in speed (Fig. S3G) but rather because
225 they moved more persistently than well-nurtured cells (Fig. 3E). Consistent with their increased
226 persistence, the movement of ischemic cells was *superdiffusive* – *i.e.* significantly more
227 directional than expected by a random walk[81] (Fig. 3F, **m**ean **s**quare **d**isplacement (MSD)
228 constant, σ=1.19; Fig. S3H). In contrast, MSD analysis of cells in well-nurtured clusters was
229 indistinguishable from a random walk (Fig. 3F, MSD constant, σ=1.02; Fig. S3H).

230 To further explore these data, we defined *runners* as cells whose net displacement was greater
231 than an arbitrary distance threshold (50μm). At most values of this threshold, ischemic clusters
232 had about twice as many runners than well-nurtured spheroids or spheroids in chambers
233 without consumer cells. Interestingly, we observed a directional bias in the movement of runner
234 cells away from ischemia as if they were moving toward nutrient sources (Fig. 3G; Fig. S3I).
235 However, this directional bias was small and only significant under some definitions (distance
236 thresholds) of runner cells (Fig. S3J). We thus concluded that – at least in this setting –
237 metabolite gradients do not act as significant orientation cues. Still, our data shows that
238 ischemia leads to more persistent movements in three-dimensional tumor cultures resulting in
239 highly dispersive and invasive tumor spheroids.

240 **Ischemic tumor cells lose epithelial features and increase ECM degradation**

241 We then sought to determine specific cell changes triggered by ischemia. From a biophysical
242 standpoint, the MSD changes observed in our cell tracking analyses, suggest that the
243 movements of ischemic cells are less constrained[82]. Typically, constrains in cell migration are
244 imposed by the ECM or by adhesion to other cells[42,43]. Consistently, hypoxic tumor cells are
245 known to increase ECM invasion[23,83] and to have lower levels of epithelial cell adhesion
246 molecules such as E-Cadherin (E-Cad)[84–90]. We thus wanted to test whether ischemic spheroids
247 increase ECM degradation and/or they show changes in cell-cell adhesion. To measure ECM
248 degradation, we first used an assay where ECM proteins are laid over a coverslip coated with
249 fluorescent gelatin[91]. More invasive clusters will break down the ECM network, and eventually
250 degrade the labeled gelatin resulting in local loss of fluorescence (Fig. 4A). With this assay we

251 observed that ischemia triggered a large increase in ECM degradation in tumor spheroids (Fig.
252 4B) and in consumer cells (Fig. S4A). As an orthogonal approach, we cultured tumor spheroids
253 in DQ-Collagen – a fluorescent but quenched form of collagen that lights up when cleaved[92]. In
254 this assay, ischemic spheroids also showed significantly higher levels of ECM degradation and
255 foci of ECM degradation often colocalized with protrusive regions within spheroids (Fig. S4B).

256 Metabolic stress in the tumor microenvironment can decrease epithelial features such as E-Cad
257 levels in carcinomas as we have previously shown in the MEMIC[71]. Consistent with these
258 previous data, immunofluorescent analysis of ischemic spheroids in the 3MIC showed a
259 dramatic decrease in E-Cad levels (Fig. 4C). We observed a similar trend using a fluorescent
260 protein driven by the promoter of E-Cad (Fig. S4C), and thus suggesting that ischemia regulates
261 E-cad at the transcriptional level. As many carcinoma cells, Lung KP show an intermediate EMT
262 status mostly epithelial features including the expression of (Fig. S4D). While in our experiments
263 we see a decrease in epithelial features, we did not observe significant changes in the levels of
264 vimentin along the 3MIC suggesting that ischemia promotes a partial EMT (Fig. S4E).
265 Interestingly, a recent study demonstrated that partial EMT in vimentin-positive carcinoma is
266 required for metastasis in triple-negative breast cancer pre-clinical models[93]. In summary, these
267 results show that ischemic cells decrease epithelial adhesion and increase the degradation of
268 the surrounding ECM.

269 **A model of persistent tumor migration in the absence of directional cues**

270 Our results are consistent with well-established evidence that tumor ischemia increase
271 migratory and invasive cell properties[11,15,17,20]. Since these conditions arise deep within tumors,
272 how do nascent metastatic cells move through the tumor tissue to eventually reach the tumor's
273 edge? An appealing hypothesis is that nutrients or oxygen act as directional cues that orient the
274 movements of ischemic cells. However, we did not find enough evidence in our data to support
275 this hypothesis (Fig. 3G; Fig. S3H,I). We thus asked whether our other observations: a
276 decrease in epithelial adhesion and increased ECM degradation are sufficient to allow the
277 escape of ischemic cells from the nutrient-deprived regions they emerge from.

278 We decided to address this question conceptually using a Cellular Potts Model[94,95] – a
279 mathematical framework frequently used to model problems of differential cell adhesion and cell

280 sorting in morphological processes[96]. In a Cellular Potts Model, any number of 'cell types' exist
281 on a grid and have different affinities for each other and for their surrounding substrate. High
282 affinity contacts have a lower surface energy and thus they are more stable. In contrast, low
283 cell-cell or cell-substrate affinities are represented as highly energetic and unstable contacts. At
284 every simulated time point (a Monte Carlo Step, MCS), the model tries to minimize the energy of
285 the system resulting in changes in cell shape, localization, etc. according to local energy
286 levels[94,95].

287 Our modeled tumors were formed by two cell types: *core* (ischemic) and *cortical* (well-perfused)
288 cells designated according to their positions at the beginning of the simulation. Our specific goal
289 was to test whether changes in cell-cell and cell-substrate adhesion would allow core cells to
290 move through cortical cells and eventually invade into the surrounding ECM. We modeled the
291 reduced levels of epithelial adhesion we observed in ischemic cells as a decreased cell-cell
292 affinity by increasing in the surface energy between core cells i.e. decreasing their stability.
293 Energy levels were set to ensure that the adhesion between core cells was low, between
294 cortical cells was high, and intermediate between the two cell types. We tested a range of
295 energy parameters obtaining similar qualitative results as long as we kept these relationships
296 (Fig. 4D; see additional details in Tables S1 and S2). Implementation of these changes resulted
297 in clusters where core cells mixed with cortical cells but there was no invasion into their
298 surroundings (Fig. 4E; Video S5). To model the increased ECM invasion in ischemic cells, we
299 increased the affinity for the surrounding ECM in core. The intuition behind this step is an
300 increase in ECM degradation will facilitate the movement of tumor cells into the ECM, which in a
301 Cellular Potts Model equates to a higher ECM-tumor affinity (Fig. S4F). This feature alone,
302 produced poor mixing between populations and a moderate trend to invade the ECM (Fig. 4E;
303 Video S5). However, cell movements were random and did not show the persistence we
304 observed in our experimental data (Fig. S4G).

305 The combination of these two rules however – core cells with decreased cell-cell adhesion and
306 increased affinity for the ECM – produced the most interesting outcomes. Ischemic core cells
307 moved through layers of well-perfused cells and rapidly dispersed through the surrounding ECM
308 (Fig. 4E; Video S5). These virtual cell movements were remarkably close to the movements of
309 our experimental cells. For example, tracks of core and cortical cells in the model (Fig. 4F),

310 resembled the movements of ischemic and well-nurtured cells, respectively (compare with Fig.
311 S3F). Most strikingly, the MSD of core cells in this scenario increased by the same order of
312 magnitude as in our experimental cells in the 3MIC (compare Fig. 4G and Fig. 3F). Altogether
313 these data suggest that increasing the affinity for the ECM and decreasing cell-cell adhesion is
314 sufficient for the spontaneous emergence of directional movements driving the dispersion of
315 core cells into the ECM – even in the absence of explicit directional cues. While many other
316 mechanisms will contribute to the translocation of ischemic tumor cells to regions from where
317 they can spread from *in vivo*, this model proposes a minimal set of conditions that can facilitate
318 this process.

319 **Pro-metastatic features induced by ischemia are reversible**

320 Hypoxic and ischemic environments can select for more aggressive and metastatic
321 clones[54,97,98]. The contribution of clonal selection in our brief 3MIC experiments (~24-72h) is
322 negligible. *In vivo* however, time scales are much longer, which may allow ischemia to select for
323 more migratory clones. We hypothesized that if ischemic cells are selected to be more migratory
324 *in vivo*, they should display a higher migratory phenotype in the 3MICs – irrespective of their
325 location along the ischemic gradient. We thus injected Lung KP cells expressing HRE-GFP into
326 the flank of syngeneic mice. After 2 weeks, we extracted these tumors and dissociated them
327 into single cells. Using flow cytometry, we sorted ischemic from non-ischemic cells according to
328 their GFP levels (Fig. S5A). From these sorted cells, we generated tumor spheroids, which we
329 then cultured into separated 3MICs (Fig. 5A; Fig. S5B). As shown in figure 5, the increase in cell
330 invasion strongly correlated with the distance to the opening but not with their precedence (Fig.
331 5B,C). Consistently, spheroids formed neither from hypoxic nor from non-hypoxic tumor cells
332 showed and increased invasion when cultured in 3MICs without consumers (Fig. S5C,D). These
333 results show that, at least in this system, the pro-metastatic features produced by ischemia are
334 phenotypic changes that do not require clonal selection.

335 **Reconstruction and visualization of more complex microenvironments**

336 Solid tumors are infiltrated by a variety of stromal and immune cells[22,29,30]. Tumor-associated
337 macrophages (TAMs) are one of the most abundant cell types in solid tumors and their
338 presence correlates with increased cancer progression, metastasis, and mortality[20,30,31,99–102].

339 TAMs recruit endothelial cells helping to orchestrate the vascularization process required for
340 tumor growth and metastasis[31]. We recently showed that a combination of hypoxia and high
341 lactic acid, activates the ERK/MAPK pathway in macrophages who then secrete VEGFA and
342 induce tube-like morphogenesis in endothelial cells[70]. To test whether we could recapitulate
343 these data in the 3MIC, we generated endothelial clusters from SVEC4-10 cells (referred as
344 SVECs) and co-cultured them with bone marrow-derived macrophages (BMDMs). As controls
345 we examined similar SVEC clusters in 3MICs without macrophages. In the absence of
346 macrophages, clusters of endothelial cells remained mostly rounded, even in the presence of
347 consumer cells and regardless of their location along the ischemic gradient (Fig. 6A). In the
348 presence of macrophages however, ischemic endothelial cells extended away from clusters and
349 sprouted into the ECM (Fig. 6A; Video S6). This tube-like morphogenesis did not occur in well-
350 nurtured regions of the 3MIC (Video S6). We did not notice that the cell type used as consumers
351 produced significant differences in endothelial sprouting, but it always required the infiltration of
352 macrophages (Fig. S6A). Consistent with previous evidence[31,70], inhibition of VEGF signaling
353 with linifanib abrogated the endothelial sprouting induced by macrophages (Fig. 6B; Fig. S6B).
354 While this inhibitor may have off target effects, these data are consistent with prior data showing
355 VEGF secretion and a pro-angiogenic role ischemic in ischemic macrophages[31,70].

356 We then co-cultured macrophages with tumor spheroids. In these experiments, we observed
357 that the presence of macrophages increased the migration and ECM invasion of tumor cells.
358 This increase was evident even in well-nurtured regions, but much stronger under ischemia
359 (Fig. 6C). Similarly, macrophages and ischemia synergized to decrease E-Cad levels (Fig. 6D).

360 Live imaging of these tumor-macrophage interactions also revealed a fascinating behavior:
361 tumor cells from ischemic spheroids extended protrusions towards macrophages appearing to
362 physically drag them into the tumor cell cluster (Fig. 6C; Video S7). This observation suggests
363 that there may be an understudied mechanical interaction where malignant cells may 'pull'
364 macrophages into the tumor. Increasing the complexity of co-cultures in the 3MIC is simple. For
365 example, we produced a triple co-culture of chimeric SVEC/Lung KP spheroids grown in ECM
366 and surrounded by macrophages (Fig. 6E; Video S8). Here again we observed the strong
367 synergy between metabolic and macrophage signals in promoting morphological changes in
368 tumor and endothelial cells.

369 **Using the 3MIC to test the effects of anti-motility drugs on ischemic cells**

370 Limited diffusion of anticancer drugs from blood vessels into solid tumors is a major therapeutic
371 challenge[103,104] (Fig. 7A). Multiple factors account for poor drug penetration including tumor
372 vascularization and the distance between blood vessels[105], simple diffusion through of cells and
373 the ECM[106], and drug consumption and degradation by cells in the tumor microenvironment[107].
374 In addition, hypoxic and ischemic cancer cells can develop drug resistance by increasing ABC
375 transporters and drug efflux[108], and bypass drug targets through metabolic rewiring[109].
376 Distinguishing biophysical limitations to drug penetration from the acquisition of true drug
377 resistance is necessary to improve therapy and yet most assays struggle to untangle these
378 factors[104]. The 3MIC can solve some of these issues providing a unique opportunity to test
379 drugs that directly target metastatic initiation.

380 To illustrate this principle, we treated tumor spheroids with anti-migratory doses of Taxol. At
381 high doses, Taxol stabilizes microtubules leading to mitotic arrest and cell death[110]. However,
382 sub-lethal concentrations of this drug inhibit migration and invasiveness in several cell
383 types[111,112] (Fig. S7A). In our experiments, we determined that concentrations of 20-200nM of
384 Taxol drastically inhibited the movements and invasion of well-nurtured KP lung spheroids with
385 no effects on their cell viability (Fig. S7B). Similar levels of this drug however, had much milder
386 effects or no effects at all on the movements of ischemic tumor spheroids (Fig. S7C).

387 To distinguish whether these differences are due to a decrease in Taxol levels along the 3MIC,
388 or if they denote a differential response in ischemic cells, we took advantage of fluorophore-
389 conjugated Taxol analogues. These compounds are routinely used to label microtubules, and
390 thus we can use the intensity of microtubule staining as a proxy for local drug levels (Fig. 7B;
391 Fig. S7D). After adding known quantities of the fluorescent Taxol analog (Taxol-Cy5),
392 fluorescence levels progressively decreased in distal spheroids, but they did so at the same rate
393 in 3MICs with or without consumer cells (Fig. 7C; Fig. S7D,E). These results indicate that
394 consumer cells have a negligible effect on the Taxol gradient. From the changes in microtube
395 staining intensity, we determined that in a 3MIC culture treated with 150nM of Taxol, the most
396 ischemic spheroids will experience about ~30nM of Taxol (45nM at 10mm and 24nM at 12mm,
397 Fig. 7C). While these Taxol levels have no effects on ischemic tumor spheroids, 30nM of this
398 drug completely inhibited the movements of well-nurtured tumor cells (Fig. 7D). We thus

399 concluded that ischemic spheroids are more resistant to Taxol by mechanisms beyond drug
400 penetration and diffusion.

401 **DISCUSSION**

402 Animal models are fundamental to study the complexity and heterogeneity of the tumor
403 microenvironment[113,114]. In these *in vivo* models however, it is hard to isolate and weigh the
404 contributions of different variables to tumor progression, and large experiments are prohibitively
405 expensive for most laboratories[61,62]. On the other hand, conventional *in vitro* approaches offer
406 much better experimental control and can be easily scaled up for high throughput approaches.
407 However, *in vitro* models do not usually consider the cellular and molecular heterogeneity of the
408 tumor microenvironment. The lack of models that can bridge the complexity of *in vivo* models
409 with the ease of *in vitro* cultures has impaired progress in understanding the tumor
410 microenvironment and how it can modulate the emergence of metastatic tumor features[2,115,116].
411 To bridge this technical gap, we described the design and implementation of the 3MIC – an *ex*
412 *vivo* culture system that allows visualizing the acquisition of metastatic-like migratory properties
413 in complex 3D tumor cultures. Altogether the experiments presented here show that the 3MIC
414 recapitulates key features of the tumor microenvironment. It allows for imaging ischemic cells
415 that are hidden to conventional techniques and permits testing the role of different elements of
416 the tumor microenvironment and the effects of drugs on the emergence of metastatic features
417 (Fig. 7E).

418 The results shown here are consistent with well-established evidence that hypoxia is essential
419 for the emergence of metastasis. The 3MIC however, allowed us to gain new insights into this
420 process by 1) re-creating a complex ischemic-like metabolic microenvironment rather than
421 simple hypoxia and 2) overcoming challenges associated with imaging ischemic cells that are
422 usually located deep within tumor structures. The ischemic-like environment formed in the 3MIC
423 better mimics metabolic conditions in tumors such as accumulation of lactic acid and nutrient
424 deprivation[52,71,117]. In our experiments, we found evidence that media acidification has a more
425 direct effect on the invasive properties of ischemic spheroids than hypoxia. We think that media
426 acidification may be the direct signal that triggers invasion under ischemia while hypoxia
427 indirectly contributes to this effect through the pro-glycolytic role of HIF1A[78]. At this moment, we
428 can only speculate why pH perturbations may have such strong effects in our experiments. A
429 possible explanation is that many ECM-digesting metalloproteases have lysosomal origins or
430 are more active in more acidic environments and thus extracellular acidification would increase

431 the efficiency of these enzymes[43,77,118]. While our data shows a critical role for hypoxia and
432 extracellular pH, additional metabolic[37,38] and non-metabolic cues are likely to increase cell
433 invasion under ischemia. For example, glucose deprivation triggers the release of pro-migratory
434 cytokines[119] and there is a growing list of metabolites that directly or indirectly affect the number
435 and destination of metastases[37,38].

436 Our data shows that ischemic cells display a more efficient dispersion. Consistent with previous
437 evidence[120,121], we showed here that ischemia decreases epithelial cell adhesion and increases
438 the degradation of the extracellular matrix. While some of our observations share features with
439 the process of epithelial-to-mesenchymal transition (EMT), we preferred referring to a partial
440 EMT as we only observed a decrease in epithelial features without a significant change in
441 mesenchymal markers. In addition, the contribution of EMT to the metastatic process remains
442 controversial[86,122,123]. An additional issue to consider is the composition of the ECM as they can
443 alter the phenotypes and behavior of tumor and stromal cells[124]. While in our experiments we
444 used a simple combination of collagen and Matrigel in our experiments, the 3MIC allows testing
445 different ECM compositions and structural scaffolds (Fig. 7E).

446 At the single-cell level, ischemia increases cell persistence without a significant change in cell
447 polarity or increasing directional cell migration. However, we observed a small bias towards
448 higher nutrients in the direction of cell movements. While in our setting these differences were
449 not statistically significant, this observation would be consistent with a widespread set of
450 examples of nutrient-driven chemotaxis in prokaryotes and in other eukaryotic cells[125,126]. For
451 example, the key nutrient sensor mTORC2 is critical in neutrophil chemotaxis. Still, additional
452 experiments will be needed to establish whether or not tumor cells can follow nutrient gradients.

453 Recent evidence shows that tumor hypoxia can act as an evolutionary pressure that selects for
454 tumor clones that are more resilient to stressors such as reactive oxygen species[86,97,127].
455 However, our data shows that hypoxia and ischemia can alter cells directly without the need for
456 clonal selection. These two ideas are not in conflict and our experimental conditions are not free
457 of caveats. Most likely the acquisition of metastatic features in patients occurs by a combination
458 of selection and opportunistic adaptations to the tumor microenvironment.

459 The direct visualization of tumor-stroma interactions afforded by the 3MIC has unique
460 advantages. For example, we were excited to observe that the movement of macrophages
461 toward tumor structures seemed to be driven by tumor cells mechanically dragging
462 macrophages into their clusters (see for example Video S7). It is possible then, that immune
463 infiltration of tumors is aided by physical recruitment by cancer cells. While we are not aware of
464 previous reports of this behavior, this may be due to the challenges of observing tumor-
465 macrophage interactions *in vivo*, especially in ischemic tumor regions.

466 It has been difficult to discern whether a decrease in drug response *in vivo* is due to lower drug
467 concentration or to intrinsic changes that make cells more drug-resistant[128]. This is particularly
468 true in more fibrotic and ischemic tumors such as pancreatic ductal adenocarcinomas[129,130]. The
469 3MIC however allows for the separation of these effects and we were able to show that
470 ischemic cells display a true Taxol resistance mechanism. These experiments illustrate the ease
471 of testing drugs on ischemic cells and untangling biophysical factors such as drug diffusion from
472 biological adaptations to anticancer drugs. While the particular example we used benefited from
473 the availability of labeled Taxol analogs, a similar approach is possible using imaging mass
474 spectrometry and other methods that allow the quantification of local drug levels[131].

475 Finally, the fabrication of the 3MIC is easy and affordable with a conventional 3D printer. This
476 system can seamlessly integrate existing co-culture and *ex vivo* protocols and thus, we invite
477 the research community to use the 3MIC when studying metastasis and other processes where
478 the limitation of nutrients in 3D multicellular structures is relevant.

479 **METHODS**

480 **Cell culture**

481 Lung KP clones and Lung KPKeap1 clones were derived from the $KRAS^{G12D}/TP53^{-/-}$ and
482 $KRAS^{G12D}/TP53^{-/-}/Keap1^{-/-}$lung adenocarcinoma model, respectively, developed and kindly
483 shared by Dr. Thales Papagiannakopoulos. MCF10A, MCF7, DID1, and SVEC-4-10 cells were
484 purchased from ATCC. C6-HRE-GFP cells were a kind gift from Dr Inna Serganova (Memorial
485 Sloan Kettering Cancer Center, New York, NY, USA). Cells were cultured in High Glucose
486 DMEM (Gibco, #11965-092) supplemented with 10% Fetal Bovine Serum (FBS; Sigma-Aldrich,
487 #F0926) at 5% CO_2 and 37°C. MCF10A cells were cultured in High Glucose DMEM (Gibco,
488 #11965-092) supplemented with 5% Horse Serum, 20ng/ml Animal-Free Recombinant Human
489 Epidermal Growth Factor (Peprotech,#AF-100-15) , 0.5 mg/ml Hydrocortisone (Sigma-Aldrich,
490 #H0888), 100 ng/ml Cholera Toxin (Sigma-Aldrich, C8052), 10µg/ml Insulin, at 5% CO_2 and
491 37°C. To induce HIF1A signaling in normal oxygen conditions, cell spheroids were treated with
492 2mM DMOG (Selleckchem, #S7483) or with 300μM $CoCl_2$ (ThermoFisher Scientific #012303-
493 30) for 18 hours. To alter the pH of the media, we added 25mM of $NaHCO_3$ (ThermoFisher
494 Scientific #25080094) or 20mM of lactic acid (Sigma #L1750) to the media.

495 Lung KP cells stably expressing a hypoxia reporter (pLenti-5XHRE-GFP, Addgene #128958,
496 denoted here as HRE-GFP), cell membrane marker (pLenti-mCherry-CAAX, Addgene
497 #129285), E-cadherin reporter (pHAGE-E-cadherin-RFP, Addgene #79603), cell cycle reporter
498 (pBOB-EF1-FastFUCCI-Puro, Addgene #86849), LV-YFP (Addgene #26000), and pLenti-H2B-
499 iRFP720 (Addgene #128961) were generated using standard lentivirus mediated stable cell line
500 preparation protocols. H2B-mCherry was cloned by removing YFP from the LV-YFP vector
501 using BamHI and KpnI restriction enzymes. The linearized vector containing H2B was then
502 ligated with mCherry using SLIC[132].

503 **Formation of 3D tumor spheroids**

504 Cell spheroids were formed via hanging drops following standard protocols[133]. Briefly, cells were
505 dissociated into a single-cell suspension of 10^4 cells/ml. The cell suspension was distributed into
506 20μl droplets onto the lid of a Petri dish. The base of the dish was filled with PBS (Gibco,

507 #14040-133) or distilled water to prevent droplet evaporation during the incubation time. The lid
508 was then inverted onto the dish and incubated for 96 hours, to ensure the formation of compact
509 spheroids. Typically, we cultured ~50 spheroids in each 3MIC chamber.

510 **Isolation and differentiation of BMDMs**

511 Bone marrow-derived macrophages (BMDMs) were extracted from C57BL/6 mice following
512 standard protocols[69,70]. Following isolation of the bone marrow, cells were cultured in low
513 attachment culture dishes (VWR, #25384-342) in High Glucose DMEM supplemented with 10%
514 FBS and 10ng/mL Recombinant Mouse CSF-1 (R&D Systems, #416-ML) for 7 days.

515 **Establishment of tumor-derived clones**

516 Approximately $5x10^4$ cells Lung KP cells, stably expressing pLenti-5XHRE-GFP and pLenti-
517 mCherry-CAAX were injected subcutaneously into C57BL/6 mice and grown for 14 days.
518 Tumors were then extracted and dissociated using a solution containing of 2U/ml Dispase and
519 4mg/ml Collagenase IV. Tumor cells were enriched as a CD45 negative population and sorted
520 to their GFP levels. GFP-positive and negative cells were grown separately as clusters using
521 the hanging drop method described above.

522 **Generation of Hif1a KO cells**

523 Hif1a knockout cells were generated using CRISPR/Cas9 genome editing. Briefly, forward and
524 reverse sequences (CACCGAGATGTGAGCTCACATTGTG and
525 AAACCACAATGTGAGCTCACATCTC) were synthesized to form single guide RNAs (sgRNAs)
526 targeting the Hif1a gene. A vector (lentiCRISPR-v2-puromycin, Addgene #98290) carrying this
527 sgRNA was introduced into HEK293T cells together with envelope and packaging plasmids
528 (VSV-G and Delta-8.9) via transfection using Lipofectamine (Thermo Scientific #L3000008).
529 Target cells were then infected with collected lentiviral particles, selected using puromycin
530 (10μg/mL Gibco #A1113803) and separated into single clones through limiting dilution.

531 **3D printing and microfabrication**

532 To create the framework of 3MIC fused filament fabrication was used. Designing of the
533 framework was done using openSCAD (https://openscad.org). 3MICs were printed in two parts
534 that were later assembled: the main framework and the upper coverslip holder (where consumer
535 cells are grown). These parts were printed in an Ultimaker 3B printer using Black PLA filament.
536 Alternatively, the framework can be printed using Stereolithography (SLA) printers. In this case,
537 the entire framework (the upper coverslip holder and main framework) can be printed as one
538 unit. We used Dental SG resin to print the framework on Form 3 (Formlabs). The uncured resin
539 was removed from the prints by washing them in isopropanol for 1 h and further post-curing it
540 with UV irradiation heated at 60°C. A glass coverslip (VWR, No. 1, 22x60mm, #48393-070) was
541 glued to the base of the main framework using a UV-curable adhesive (Norland Products,
542 NOA68) using a long-wave UV lamp (MelodySusie, DR-5401). Then, the coverslip holder
543 fragment was glued onto the glass coverslip. Finally, the assembled 3MIC was sterilized in a
544 short-wave UV lamp chamber (Meishida, CM-2009) for 15 minutes.

545 **Culture of tumor spheroids in the 3MIC**

546 To prepare the layer of consumer cells, 24hrs before the day of the experiment, a coverslip
547 (VWR #48366-045) was coated with Poly-D-lysine (Sigma-Aldrich, #P6407) to aid adherence of
548 cells to the glass surface. Cells were detached using trypsin and diluted into a cell suspension
549 of a density of $3.5x10^5$ cells/mL for faster dividing cells and 10^6 cells/mL for slower dividing cells.
550 The coverslip was placed into a well of a 6-well dish and covered with 1mL of the cell
551 suspension. The coverslip was incubated overnight at 37°C to let the cells adhere to the
552 coverslip. On the day of the experiment, the spheroids were collected from the Petri dishes by
553 inverting the lid and gently flushing all the spheroids with DMEM supplemented with 10% FBS
554 using a 5mL serological pipette. The spheroid containing suspension was collected and
555 centrifuged at 50G for 10-15 minutes. Meanwhile, a thin bed of 110μL ECM was made in the
556 3MIC – here, we used either 2.2mg/mL rat tail Collagen (Corning, #354236) – or 2:3 mix of
557 Matrigel and 1.6mg/ml of rat tail Collagen I and incubated at 37°C for 20 mins to allow the
558 polymerization of the ECM. Spheroids were resuspended in about 110μL of ECM and
559 immediately transferred onto the polymerized ECM bed. The ECM with spheroids was
560 polymerized at 37°C for ~30 minutes. With the help of forceps, the coverslip containing the
561 consumer cells was inverted and inserted into the slot of the coverslip holder. The 3MIC was

562 then gently filled with 1.25mL of media, avoiding trapping bubbles underneath the consumer
563 coverslip. Control wells are assembled in the same way, but the top coverslip has no consumer
564 cells.

565 **Collagen degradation assay**

566 To investigate the invasive potential of cells across the gradient, the ECM was mixed with DQ-
567 collagen, type I From Bovine Skin, Fluorescein Conjugate (Invitrogen, #D12060) at a final
568 concentration of 25*μ*g/ml. This ECM was used to prepare the bed and embed the spheroids as
569 well. The extent of degradation of the matrix was determined by measuring the fluorescence
570 intensity of cleaved collagen.

571 **Gelatin degradation assay**

572 Glass coverslips were coated with gelatin from pig skin, Oregon Green 488 Conjugate (Thermo
573 Fisher Scientific, #G13186), by inverting coverslips on 20µl drops of fluorescent gelatin
574 (1mg/ml) and incubating for 20 minutes. The coverslips were then lifted, excess liquid drained,
575 and inverted on 40µl drops of 0.5% glutaraldehyde for fixation. The coverslips were then
576 washed with PBS and glued onto the PLA frame using the UV-curable adhesive (Norland
577 Products, #NOA68) and cured in a long-wave UV lamp (MelodySusie, #DR-5401) for 15
578 minutes. The cured coverslip was then UV-sterilized and used for the experiment. Briefly, the
579 spheroids were collected from the hanging drops and centrifuged and resuspended in 100µl of
580 media. The spheroid solution was carefully placed on the coated coverslips and incubated for
581 30-60 minutes to allow the spheroids to settle down. After ensuring that there are no floating
582 spheroids, the consumer coverslip was transferred into the 3MIC and the remaining 1.4ml of
583 media was added. The 3MICs were incubated at 37°C, for 24 hours. After 24 hours, the 3MICs
584 were fixed using 4% paraformaldehyde (PFA) for 10 mins and imaged using 10X objective of
585 Nikon Eclipse Ti2-E spinning disk confocal microscope.

586 **Microscopy**

587 Microscopic images were captured using a 10x objective of Nikon Eclipse Ti2-E spinning disk
588 confocal microscope, at fixed timepoints or set up for time-lapse microscopy. For time-lapse
589 microscopy, cells were maintained at 37°C using a stage top incubator (Tokai Hit, #INUCG2-

590 KRi) and the chamber was connected to a humidified mixed gas source (5% CO_2). Spheroids
591 from different regions of the 3MIC were imaged at suitable time-intervals in different fluorescent
592 channels. Typically, we imaged ~10 spheroids per 3MIC every 15-30 mins for 24h. Extracellular
593 pH was estimated using the ratio of the green over the blue channels one RGB images of cell
594 culture media containing the pH indicator phenol red. As pH decreases and the media yellows,
595 the signal on the green channel increases while the blue channel remains largely unchanged.
596 To match this ratio to specific pH values, we imaged and measured the pH of the same culture
597 media supplemented with different levels of lactic acid.

598 **Immunofluorescence**

599 Spheroids within the 3MIC were fixed using 4% PFA (Affymetrix, #19943) for 10 minutes at
600 room temperature and washed four times with PBS. Cultures were permeabilized using PBS
601 containing 0.5% (vol/vol) Triton-X-100 (Sigma-Aldrich, #T8787) for 20 minutes and washed
602 three times with PBS. Slides were blocked in 10% FBS in immunofluorescence (IF) buffer (0.3M
603 glycine in PBS) for 60 minutes at room temperature. Primary antibodies were diluted at 1:200 in
604 the same blocking solution. We used anti-phospho-H3 (Cell Signaling Technologies, #9706), E-
605 cadherin (BD Bio Sciences, #610182), and CD45 (R&D, #AF114) antibodies. 3MICs were
606 incubated with primary antibodies overnight at 4°C, then washed with IF buffer and incubated
607 overnight at 4°C with secondary antibodies also diluted in blocking solution at 1:200. Cultures
608 were then washed and counterstained with 0.5µg/mL Hoechst 33342 in PBS (Invitrogen,
609 #H1399).

610 **Image analysis**

611 Automated cell tracking was conducted as previously described[69]. Persistence is defined as the
612 ratio between the net displacement of a cell over its trajectory. We estimated the local cell
613 density using a method based on the Delaunay triangulation of neighboring cells[69,70]. Per cell,
614 per spheroid, and population levels of florescence were estimated using custom image analysis
615 software as previously described[71].

616 **Cellular Potts Model (CPM) simulations**

617 Simulations were conducted using a MATLAB CPM implementation[134]. Adhesion between core
618 (C1) and cortical (C2) cells were implemented as:

619 $$J_{C1,C1} > J_{C1,C2} > J_{C2,C2}$$

620 Where $J_{i,j}$ is the surface energy at every contact point between the two cells[95]. This relationship
621 modeled the decrease in E-Cad levels in ischemic cells. The differential affinity for the ECM in
622 core cells was simulates as:

623 $$J_{C1,ECM} < J_{C2,ECM}$$

624 The CPM was implemented in a 200x200 grid with 100 initial cells and run for $1{,}28 \times 10^8$ Monte
625 Carlo Simulation steps. Parameters used in the conditions presented here can be found in
626 Tables S1 and S2. MATLAB routines to run the simulations are available upon request.

627 **Statistics**

628 We conducted at least three biological replicates of all experiments, unless stated otherwise.
629 Unless noted, we used two-tailed t-student tests to estimate p-values between two conditions
630 and Pearson's linear coefficient when testing correlations. For multiple comparisons, we used
631 one-way ANOVA followed by a Tukey-Kramer test. In all plots, error bars show standard
632 deviation from the mean. In boxplots, center lines show the median and box edges show 75th
633 and 25th empirical quartiles of the data.

634 **ACKNOWLEDGEMENTS**

635 We thank all members of the Carmofon Laboratory for critical discussions about this project and
636 the manuscript. This work was supported by awards to CC-F from the National Cancer Institute
637 of NIH (DP2 CA250005) and the American Cancer Society (RSG-21-179-01-TBE). CC-F is a
638 Pew Scholar in the Biomedical Sciences, supported by The Pew Charitable Trust (00034121).
639 JG was supported by a NIH Training Grant (1T32GM132037-01).

640 **Authors contributions:** Concept and experimental design CC-F with help from LA.
641 Experiments by LA, JG, JL, MR, and C-CF. Image analysis: CC-F, LA, and LJ. Mathematical
642 modeling: CC-F. Manuscript written by CC-F with feedback and contributions from all authors.

643 **Competing interests:** NYU holds a patent for the 3MIC and related systems where CC-F is the
644 inventor.

645 **Data and materials availability:** All data is available in the manuscript or the supplementary
646 materials. Original raw files and analysis software are available upon request. Use of the 3MIC
647 requires a Material Transfer Agreement and it is free for non-commercial and academic uses.

648 **ADDITIONAL INFORMATION**

649 Supplementary information is available for this paper. Correspondence and requests for
650 materials should be addressed to CC-F.

1. Siegel Mph, R. L., Giaquinto, A. N., Ahmedin, I, Dvm, J. & Siegel, R. L. Cancer statistics, 2024. *CA Cancer J Clin* **74**, 12–49 (2024).

2. Ganesh, K. & Massagué, J. Targeting metastatic cancer. *Nat Med* **27**, 34–44 (2021).

3. Li, J. *et al.* Metastasis and immune evasion from extracellular cgamp hydrolysis. *Cancer Discov* **11**, 1212–1227 (2021).

4. Aceto, N. *et al.* Circulating Tumor Cell Clusters Are Oligoclonal Precursors of Breast Cancer Metastasis. *Cell* **158**, 1110–1122 (2014).

5. Borriello, L. *et al.* Primary tumor associated macrophages activate programs of invasion and dormancy in disseminating tumor cells. *Nat Commun* **13**, 1–19 (2022).

6. Coffelt, S. B. *et al.* IL-17-producing γδ T cells and neutrophils conspire to promote breast cancer metastasis. *Nature* **522**, 345–348 (2015).

7. Gong, Z. *et al.* Immunosuppressive reprogramming of neutrophils by lung mesenchymal cells promotes breast cancer metastasis. *Sci Immunol* **8**, (2023).

8. Hu, J. *et al.* STING inhibits the reactivation of dormant metastasis in lung adenocarcinoma. *Nature* **616**, 806–813 (2023).

9. Bakker, G. J. *et al.* Intravital deep-tumor single-beam 3-photon, 4-photon, and harmonic microscopy. *Elife* **11**, (2022).

10. Wyckoff, J. B., Jones, J. G., Condeelis, J. S. & Segall, J. E. A Critical Step in Metastasis: In Vivo Analysis of Intravasation at the Primary Tumor 1. *Cancer Res* **60**, 2504–2511 (2000).

11. Nakasone, E. S. *et al.* Imaging Tumor-Stroma Interactions during Chemotherapy Reveals Contributions of the Microenvironment to Resistance. *Cancer Cell* **21**, 488–503 (2012).

12. Iacobuzio-Donahue, C. A. *et al.* Cancer biology as revealed by the research autopsy. *Nat Rev Cancer* **19**, 686–697 (2019).

13. Ring, A., Nguyen-Sträuli, B. D., Wicki, A. & Aceto, N. Biology, vulnerabilities and clinical applications of circulating tumour cells. *Nat Rev Cancer* (2022) doi:10.1038/S41568-022-00536-4.

14. Kumar, A. *et al.* Substantial interindividual and limited intraindividual genomic diversity among tumors from men with metastatic prostate cancer. *Nat Med* **22**, 369–378 (2016).

15. Brown, D. *et al.* Phylogenetic analysis of metastatic progression in breast cancer using somatic mutations and copy number aberrations. *Nat Commun* **8**, 1–13 (2017).

16. Hoadley, K. A. *et al.* Tumor Evolution in Two Patients with Basal-like Breast Cancer: A Retrospective Genomics Study of Multiple Metastases. *PLoS Med* **13**, e1002174 (2016).

17. Padmanaban, V. *et al.* E-cadherin is required for metastasis in multiple models of breast cancer. *Nature* **573**, 439–444 (2019).

18. Gkountela, S. *et al.* Circulating Tumor Cell Clustering Shapes DNA Methylation to Enable Metastasis Seeding. *Cell* **176**, 98-112.e14 (2019).

19. Harper, K. L. *et al.* Mechanism of early dissemination and metastasis in Her2+ mammary cancer. *Nature* **540**, 588–592 (2016).

20. Linde, N. *et al.* Macrophages orchestrate breast cancer early dissemination and metastasis. *Nat Commun* **9**, 21 (2018).

21. Hosseini, H. *et al.* Early dissemination seeds metastasis in breast cancer. *Nature* **540**, 552–558 (2016).

22. Massagué, J. & Ganesh, K. Metastasis-Initiating Cells and Ecosystems. *Cancer Discov* **11**, 971–994 (2021).

23. Rankin, E. B. & Giaccia, A. J. Hypoxic control of metastasis. *Science (1979)* **352**, 175–80 (2016).

24. Gilkes, D. M., Semenza, G. L. & Wirtz, D. Hypoxia and the extracellular matrix: drivers of tumour metastasis. *Nat Rev Cancer* **14**, 430–439 (2014).

25. Nobre, A. R., Entenberg, D., Wang, Y., Condeelis, J. & Aguirre-Ghiso, J. A. The Different Routes to Metastasis via Hypoxia-Regulated Programs. *Trends Cell Biol* **28**, 941–956 (2018).

26. Klein, C. A. Parallel progression of primary tumours and metastases. *Nat Rev Cancer* **9**, 302–312 (2009).

27. Makohon-Moore, A. P. *et al.* Precancerous neoplastic cells can move through the pancreatic ductal system. *Nature* **561**, 201–205 (2018).

28. Chen, L. L., Blumm, N., Christakis, N. A., Barabási, A. L. & Deisboeck, T. S. Cancer metastasis networks and the prediction of progression patterns. *Br J Cancer* **101**, 749–758 (2009).

29. Quail, D. F. & Joyce, J. A. Microenvironmental regulation of tumor progression and metastasis. *Nat Med* **19**, 1423–1437 (2013).

30. Condeelis, J. & Pollard, J. W. Macrophages: Obligate Partners for Tumor Cell Migration, Invasion, and Metastasis. *Cell* **124**, 263–266 (2006).

31. Wenes, M. *et al.* Macrophage Metabolism Controls Tumor Blood Vessel Morphogenesis and Metastasis. *Cell Metab* **24**, 701–715 (2016).

32. Wyckoff, J. B. *et al.* Direct Visualization of Macrophage-Assisted Tumor Cell Intravasation in Mammary Tumors. *Cancer Res* **67**, 2649–2656 (2007).

33. Gaggioli, C. *et al.* Fibroblast-led collective invasion of carcinoma cells with differing roles for RhoGTPases in leading and following cells. *Nature Cell Biology 2007 9:12* **9**, 1392–1400 (2007).

34. Bremnes, R. M. *et al.* The Role of Tumor Stroma in Cancer Progression and Prognosis: Emphasis on Carcinoma-Associated Fibroblasts and Non-small Cell Lung Cancer. *Journal of Thoracic Oncology* **6**, 209–217 (2011).

35. Labernadie, A. *et al.* A mechanically active heterotypic E-cadherin/N-cadherin adhesion enables fibroblasts to drive cancer cell invasion. *Nature Cell Biology 2017 19:3* **19**, 224–237 (2017).

36. Dang, H. *et al.* Cancer-Associated Fibroblasts Are Key Determinants of Cancer Cell Invasion in the Earliest Stage of Colorectal Cancer. *Cell Mol Gastroenterol Hepatol* **16**, 107 (2023).

37. Bergers, G. & Fendt, S. M. The metabolism of cancer cells during metastasis. *Nat Rev Cancer* **21**, 162–180 (2021).

38. Lehúede, C., Dupuy, F., Rabinovitch, R., Jones, R. G. & Siegel, P. M. Metabolic plasticity as a determinant of tumor growth and metastasis. *Cancer Res* **76**, 5201–5208 (2016).

39. Bergers, G. & Benjamin, L. E. Tumorigenesis and the angiogenic switch. *Nat Rev Cancer* **3**, 401–410 (2003).

40. Krishnamachary, B. *et al.* Regulation of Colon Carcinoma Cell Invasion by Hypoxia-Inducible Factor 1. *Cancer Res* **63**, 1138–1143 (2003).

41. Zhong, H. *et al.* Overexpression of Hypoxia-inducible Factor 1 in Common Human Cancers and Their Metastases 1. *Cancer Res* **59**, 5830–5835 (1999).

42. Lin, S. *et al.* Fascin promotes lung cancer growth and metastasis by enhancing glycolysis and PFKFB3 expression. *Cancer Lett* **518**, 230–242 (2021).

43. Robey, I. F. *et al.* Bicarbonate increases tumor pH and inhibits spontaneous metastases. *Cancer Res* **69**, 2260–2268 (2009).

44. Cappellesso, F. *et al.* Targeting the bicarbonate transporter SLC4A4 overcomes immunosuppression and immunotherapy resistance in pancreatic cancer. *Nat Cancer* **3**, 1464–1483 (2022).

45. Wong, C. C. L. *et al.* Hypoxia-inducible factor 1 is a master regulator of breast cancer metastatic niche formation. *Proc Natl Acad Sci U S A* **108**, 16369–16374 (2011).

46. Gatenby, R. A. & Gillies, R. J. A microenvironmental model of carcinogenesis. *Nat Rev Cancer* **8**, 56–61 (2008).

47. Lyssiotis, C. A. & Kimmelman, A. C. Metabolic Interactions in the Tumor Microenvironment. *Trends Cell Biol* **27**, 863–875 (2017).

48. Hobson-Gutierrez, S. A. & Carmona-Fontaine, C. The metabolic axis of macrophage and immune cell polarization. *Dis Model Mech* **11**, dmm034462 (2018).

49. Bader, J. E., Voss, K. & Rathmell, J. C. Targeting Metabolism to Improve the Tumor Microenvironment for Cancer Immunotherapy. *Mol Cell* **78**, 1019–1033 (2020).

50. Gatenby, R. A. & Gillies, R. J. Why do cancers have high aerobic glycolysis? *Nat Rev Cancer* **4**, 891–899 (2004).

51. Thomlinson, R. H. Hypoxia and tumours. *J Clin Pathol* **11**, 105–113 (1977).

52. Vaupel, P., Kallinowski, F. & Okunieff, P. Blood flow, oxygen and nutrient supply, and metabolic microenvironment of human tumors: a review. *Cancer Res* **49**, 6449–65 (1989).

53. Gillies, R. J. & Gatenby, R. A. Hypoxia and adaptive landscapes in the evolution of carcinogenesis. *Cancer and Metastasis Reviews* **26**, 311–317 (2007).

54. Tasdogan, A., Ubellacker, J. M. & Morrison, S. J. Redox regulation in cancer cells during metastasis. *Cancer Discov* **11**, 2682–2692 (2021).

55. Fais, S., Venturi, G. & Gatenby, B. Microenvironmental acidosis in carcinogenesis and metastases: new strategies in prevention and therapy. *Cancer and Metastasis Reviews* **33**, 1095–1108 (2014).

56. García-Jiménez, C. & Goding, C. R. Starvation and Pseudo-Starvation as Drivers of Cancer Metastasis through Translation Reprogramming. *Cell Metab* **29**, 254–267 (2019).

57. Boj, S. F. *et al.* Organoid Models of Human and Mouse Ductal Pancreatic Cancer. *Cell* **160**, 324–338 (2015).

58. Gao, D. *et al.* Organoid Cultures Derived from Patients with Advanced Prostate Cancer. *Cell* **159**, 176–187 (2014).

59. Neal, J. T. *et al.* Organoid Modeling of the Tumor Immune Microenvironment. *Cell* **175**, 1972-1988.e16 (2018).

60. Tuveson, D. & Clevers, H. Cancer modeling meets human organoid technology. *Science (1979)* **364**, 952–955 (2019).

61. Vlachogiannis, G. *et al.* Patient-derived organoids model treatment response of metastatic gastrointestinal cancers. *Science (1979)* **359**, 920–926 (2018).

62. Kopper, O. *et al.* An organoid platform for ovarian cancer captures intra- and interpatient heterogeneity. *Nat Med* **25**, 838–849 (2019).

63. Jacob, F. *et al.* A Patient-Derived Glioblastoma Organoid Model and Biobank Recapitulates Inter- and Intra-tumoral Heterogeneity. *Cell* **180**, 188-204.e22 (2020).

64. Guillen, K. P. *et al.* A human breast cancer-derived xenograft and organoid platform for drug discovery and precision oncology. *Nat Cancer* **3**, 232–250 (2022).

65. Anguiano, M. *et al.* Characterization of three-dimensional cancer cell migration in mixed collagen-Matrigel scaffolds using microfluidics and image analysis. *PLoS One* **12**, e0171417 (2017).

66. Edmondson, R., Broglie, J. J., Adcock, A. F. & Yang, L. Three-dimensional cell culture systems and their applications in drug discovery and cell-based biosensors. *Assay Drug Dev Technol* **12**, 207–218 (2014).

67. Anguiano, M. *et al.* The use of mixed collagen-Matrigel matrices of increasing complexity recapitulates the biphasic role of cell adhesion in cancer cell migration: ECM sensing, remodeling and forces at the leading edge of cancer invasion. *PLoS One* **15**, e0220019 (2020).

68. Cavo, M. *et al.* A new cell-laden 3D Alginate-Matrigel hydrogel resembles human breast cancer cell malignant morphology, spread and invasion capability observed “in vivo”. *Sci Rep* **8**, 1–12 (2018).

69. Carmona-Fontaine, C. *et al.* Emergence of spatial structure in the tumor microenvironment due to the Warburg effect. *Proceedings of the National Academy of Sciences* **110**, 19402–19407 (2013).

70. Carmona-Fontaine, C. *et al.* Metabolic origins of spatial organization in the tumor microenvironment. *Proceedings of the National Academy of Sciences* **114**, 2934–2939 (2017).

71. Janská, L. *et al.* The MEMIC is an ex vivo system to model the complexity of the tumor microenvironment. *DMM Disease Models and Mechanisms* **14**, dmm048942 (2021).

72. Sánchez-Rivera, F. J. *et al.* Rapid modelling of cooperating genetic events in cancer through somatic genome editing. *Nature* **516**, 428–431 (2014).

73. Serganova, I. *et al.* Metabolic imaging: A link between lactate dehydrogenase A, lactate, and tumor phenotype. *Clinical Cancer Research* **17**, (2011).

74. Chan, D. A., Sutphin, P. D., Denko, N. C. & Giaccia, A. J. Role of Prolyl Hydroxylation in Oncogenically Stabilized Hypoxia-inducible Factor-1α. *Journal of Biological Chemistry* **277**, 40112–40117 (2002).

75. Cox, M. E. & Dunn, B. Oxygen diffusion in poly(dimethyl siloxane) using fluorescence quenching. I. Measurement technique and analysis. *J Polym Sci A Polym Chem* **24**, 621–636 (1986).

76. Martínez-Zaguilán, R. *et al.* Acidic pH enhances the invasive behavior of human melanoma cells. *Clin Exp Metastasis* **14**, 176–186 (1996).

77. Cappellesso, F. *et al.* Targeting the bicarbonate transporter SLC4A4 overcomes immunosuppression and immunotherapy resistance in pancreatic cancer. *Nature Cancer 2022 3:12* **3**, 1464–1483 (2022).

78. Lum, J. J. *et al.* The transcription factor HIF-1α plays a critical role in the growth factor-dependent regulation of both aerobic and anaerobic glycolysis. *Genes Dev* **21**, 1037–1049 (2007).

79. Trepat, X. *et al.* Physical forces during collective cell migration. *Nature Physics 2009 5:6* **5**, 426–430 (2009).

80. Deforet, M., Carmona-Fontaine, C., Korolev, K. S. & Xavier, J. B. Evolution at the edge of expanding populations. *American Naturalist* **194**, 291–305 (2019).

81. Wu, P. H., Giri, A., Sun, S. X. & Wirtz, D. Three-dimensional cell migration does not follow a random walk. *Proc Natl Acad Sci U S A* **111**, 3949–3954 (2014).

82. Mardia, K. V. & Jupp, P. E. *Directional Statistics*. (J. Wiley, 2000).

83. Moon, E. J. *et al.* The HIF target MAFF promotes tumor invasion and metastasis through IL11 and STAT3 signaling. *Nat Commun* **12**, 1–18 (2021).

84. Polyak, K. & Weinberg, R. A. Transitions between epithelial and mesenchymal states: acquisition of malignant and stem cell traits. *Nat Rev Cancer* **9**, 265–273 (2009).

85. Scheel, C., Onder, T., Karnoub, A., Weinberg, R. A. & Talmadge, J. E. Adaptation versus Selection: The Origins of Metastatic Behavior. *Cancer Res* **67**, 11476–11480 (2007).

86. Padmanaban, V. *et al.* E-cadherin is required for metastasis in multiple models of breast cancer. *Nature* **573**, 439–444 (2019).

87. Chen, J., Imanaka, N., Chen, J. & Griffin, J. D. Hypoxia potentiates Notch signaling in breast cancer leading to decreased E-cadherin expression and increased cell migration and invasion. *British Journal of Cancer 2010 102:2* **102**, 351–360 (2009).

88. Dongre, A. & Weinberg, R. A. New insights into the mechanisms of epithelial–mesenchymal transition and implications for cancer. *Nat Rev Mol Cell Biol* **20**, 69–84 (2018).

89. Lehmann, S. *et al.* Hypoxia Induces a HIF-1-Dependent Transition from Collective-to-Amoeboid Dissemination in Epithelial Cancer Cells. *Current Biology* **27**, 392–400 (2017).

90. Jiang, L. *et al.* Metabolic reprogramming during TGFβ1-induced epithelial-to-mesenchymal transition. *Oncogene* **34**, 3908–3916 (2014).

91. Ros, M. *et al.* ER-resident oxidoreductases are glycosylated and trafficked to the cell surface to promote matrix degradation by tumour cells. *Nat Cell Biol* **22**, 1371–1381 (2020).

92. Sloane, B. F., Sameni, M., Podgorski, I., Cavallo-Medved, D. & Moin, K. Functional Imaging of Tumor Proteolysis. *Annu Rev Pharmacol Toxicol* **46**, 301–315 (2006).

93. Grasset, E. M. *et al.* Triple-negative breast cancer metastasis involves complex epithelial-mesenchymal transition dynamics and requires vimentin. *Sci Transl Med* **14**, 7571 (2022).

94. Glazier, J. A. & Graner, F. Simulation of the differential adhesion driven rearrangement of biological cells. *Phys Rev E* **47**, 2128 (1993).

95. Graner, F. & Glazier, J. A. Simulation of biological cell sorting using a two-dimensional extended Potts model. *Phys Rev Lett* **69**, 2013 (1992).

96. Szabó, A. & Merks, R. M. H. Cellular Potts modeling of tumor growth, tumor invasion, and tumor evolution. *Front Oncol* **3 APR**, 87 (2013).

97. Godet, I. *et al.* Fate-mapping post-hypoxic tumor cells reveals a ROS-resistant phenotype that promotes metastasis. *Nat Commun* **10**, 4862 (2019).

98. Labuschagne, C. F., Cheung, E. C., Blagih, J., Domart, M. C. & Vousden, K. H. Cell Clustering Promotes a Metabolic Switch that Supports Metastatic Colonization. *Cell Metab* **30**, 720-734.e5 (2019).

99. Gocheva, V. *et al.* IL-4 induces cathepsin protease activity in tumor-associated macrophages to promote cancer growth and invasion. *Genes Dev* **24**, 241–255 (2010).

100. Colegio, O. R. *et al.* Functional polarization of tumour-associated macrophages by tumour-derived lactic acid. *Nature* **513**, 559–563 (2014).

101. Noy, R. & Pollard, J. W. Tumor-Associated Macrophages: From Mechanisms to Therapy. *Immunity* **41**, 49–61 (2014).

102. Bronte, V. & Murray, P. J. Understanding local macrophage phenotypes in disease: modulating macrophage function to treat cancer. *Nat Med* **21**, 117–119 (2015).

103. Tannock, I. F., Lee, C. M., Tunggal, J. K., Cowan, D. S. M. & Egorin, M. J. Limited Penetration of Anticancer Drugs through Tumor Tissue: A Potential Cause of Resistance of Solid Tumors to Chemotherapy 1.

104. Minchinton, A. I. & Tannock, I. F. Drug penetration in solid tumours. *Nature Reviews Cancer 2006 6:8* **6**, 583–592 (2006).

105. Jain, R. K. Delivery of Molecular and Cellular Medicine to Solid Tumors. *Microcirculation* **4**, 1–23 (1997).

106. Brown, E. *et al.* Dynamic imaging of collagen and its modulation in tumors in vivo using second-harmonic generation. *Nature Medicine 2003 9:6* **9**, 796–800 (2003).

107. Shree, T. *et al.* Macrophages and cathepsin proteases blunt chemotherapeutic response in breast cancer. *Genes Dev* **25**, 2465–2479 (2011).

108. Robey, R. W. *et al.* Revisiting the role of ABC transporters in multidrug-resistant cancer. *Nature Reviews Cancer 2018 18:7* **18**, 452–464 (2018).

109. Pranzini, E., Pardella, E., Paoli, P., Fendt, S. M. & Taddei, M. L. Metabolic Reprogramming in Anticancer Drug Resistance: A Focus on Amino Acids. *Trends Cancer* **7**, 682–699 (2021).

110. Weaver, B. A. How Taxol/paclitaxel kills cancer cells. *Mol Biol Cell* **25**, 2677–2681 (2014).

111. Belotti, D. *et al.* Paclitaxel (Taxol(R)) Inhibits Motility of Paclitaxel-resistant Human Ovarian Carcinoma Cells'. *Clinical Cancer Research* **2**, 1725–1730 (1996).

112. Wang, X., Decker, C. C., Zechner, L., Krstin, S. & Wink, M. In vitro wound healing of tumor cells: Inhibition of cell migration by selected cytotoxic alkaloids. *BMC Pharmacol Toxicol* **20**, 1–12 (2019).

113. Day, C. P., Merlino, G. & Van Dyke, T. Preclinical Mouse Cancer Models: A Maze of Opportunities and Challenges. *Cell* **163**, 39–53 (2015).

114. Gould, S. E., Junttila, M. R. & Sauvage, F. J. de. Translational value of mouse models in oncology drug development. *Nat Med* **21**, 431–9 (2015).

115. Anderson, R. L. *et al.* A framework for the development of effective anti-metastatic agents. *Nat Rev Clin Oncol* **16**, 185–204 (2018).

116. Fontebasso, Y. & Dubinett, S. M. Drug Development for Metastasis Prevention. *Crit Rev Oncog* **20**, 449–474 (2015).

117. Hobson-Gutierrez, S. A. & Carmona-Fontaine, C. The metabolic axis of macrophage and immune cell polarization. *DMM Disease Models and Mechanisms* **11**, (2018).

118. Rozhin, J., Sameni, M., Ziegler, G. & Sloane, B. F. Pericellular pH affects distribution and secretion of cathepsin B in malignant cells. *Cancer Res* **54**, 6517–6525 (1994).

119. Püschel, F. *et al.* Starvation and antimetabolic therapy promote cytokine release and recruitment of immune cells. *Proc Natl Acad Sci U S A* **117**, 9932–9941 (2020).

120. Lee, J. G. *et al.* Intronic regulation of matrix metalloproteinase-2 revealed by in vivo transcriptional analysis in ischemia. *Proc Natl Acad Sci U S A* **102**, 16345–16350 (2005).

121. Chaturvedi, M. & Kaczmarek, L. MMP-9 Inhibition: a Therapeutic Strategy in Ischemic Stroke. *Mol Neurobiol* **49**, 563–573 (2013).

122. Chen, J., Imanaka, N., Chen, J. & Griffin, J. D. Hypoxia potentiates Notch signaling in breast cancer leading to decreased E-cadherin expression and increased cell migration and invasion. *Br J Cancer* **102**, 351–60 (2009).

123. Fischer, K. R. *et al.* Epithelial-to-mesenchymal transition is not required for lung metastasis but contributes to chemoresistance. *Nature* **527**, 472–6 (2015).

124. Zhang, W. J. *et al.* The reconstruction of lung alveolus-like structure in collagen-matrigel/microcapsules scaffolds in vitro. *J Cell Mol Med* **15**, 1878–1886 (2011).

125. Wadhams, G. H. & Armitage, J. P. Making sense of it all: bacterial chemotaxis. *Nat Rev Mol Cell Biol* **5**, 1024–1037 (2004).

126. Gerisch, G. Chemotaxis in Dictyostelium. *Annu Rev Physiol* **Vol. 44**, 535–552 (2003).

127. Labuschagne, C. F., Cheung, E. C., Blagih, J., Domart, M.-C. & Vousden, K. H. Cell Clustering Promotes a Metabolic Switch that Supports Metastatic Colonization. *Cell Metab* **30**, 720-734.e5 (2019).

128. Dewhirst, M. W. & Secomb, T. W. Transport of drugs from blood vessels to tumour tissue. *Nat Rev Cancer* **17**, 738–750 (2017).

129. Teicher, B. A. Hypoxia and drug resistance. *Cancer and Metastasis Reviews* **13**, 139–168 (1994).

130. Rohwer, N. & Cramer, T. Hypoxia-mediated drug resistance: Novel insights on the functional interaction of HIFs and cell death pathways. *Drug Resistance Updates* **14**, 191–201 (2011).

131. Alexandrov, T. Spatial Metabolomics and Imaging Mass Spectrometry in the Age of Artificial Intelligence. *Annu Rev Biomed Data Sci* **16**, 40 (2020).

132. Jeong, J. Y. *et al.* One-step sequence-and ligation-independent cloning as a rapid and versatile cloning method for functional genomics Studies. *Appl Environ Microbiol* **78**, 5440–5443 (2012).

133. Vinci, M., Box, C., Zimmermann, M. & Eccles, S. A. Tumor spheroid-based migration assays for evaluation of therapeutic agents. *Methods in Molecular Biology* **986**, 253–266 (2013).

134. Tsuyoshi Hirashima. Primer for cellular Potts model. *https://www.mathworks.com/matlabcentral/fileexchange/64207-primer-for-cellular-potts-model*.

FIGURES

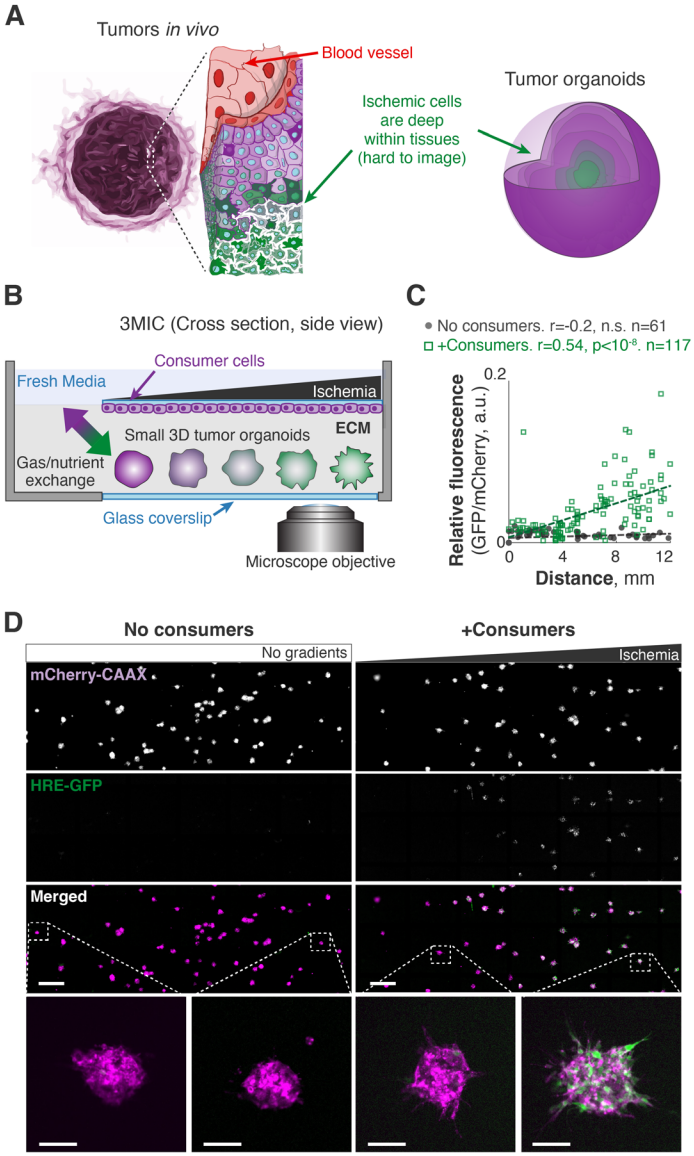

Figure 1: Design and implementation of a metabolic microenvironment chamber for 3D cultures
A. Sketch showing ischemic regions in solid tumor and conventional tumor organoids. Cells in these regions are hard to access and to image.
B. Schematic cross-section of the 3MIC where a monolayer of "consumer" cells grows on the top of a small chamber. Tumor spheroids grow embedded in ECM within the same chamber and underneath consumer cells. This small chamber is connected to a large reservoir of fresh media from only one side (left) where nutrient and gas exchanges occur.
C. Quantification of *per* spheroid GFP levels from HRE-GFP Lung KP 3D spheroids cultured in the 3MIC (~100cells/spheroid) with or without consumer cells. GFP levels serve as a proxy for hypoxia and are normalized to constitutive mCherry-CAAX signal. Dashed line: linear fit. Data from a representative example of four biological replicates.

D. Low magnification showing GFP and mCherry fluorescence in tumor spheroids cultured alone (left column) or in the presence of consumer cells (right column) along the 3MIC gradient. Bottom panels zoom into representative individual tumor spheroids. Bars: 1000μm, 100μm for insets.

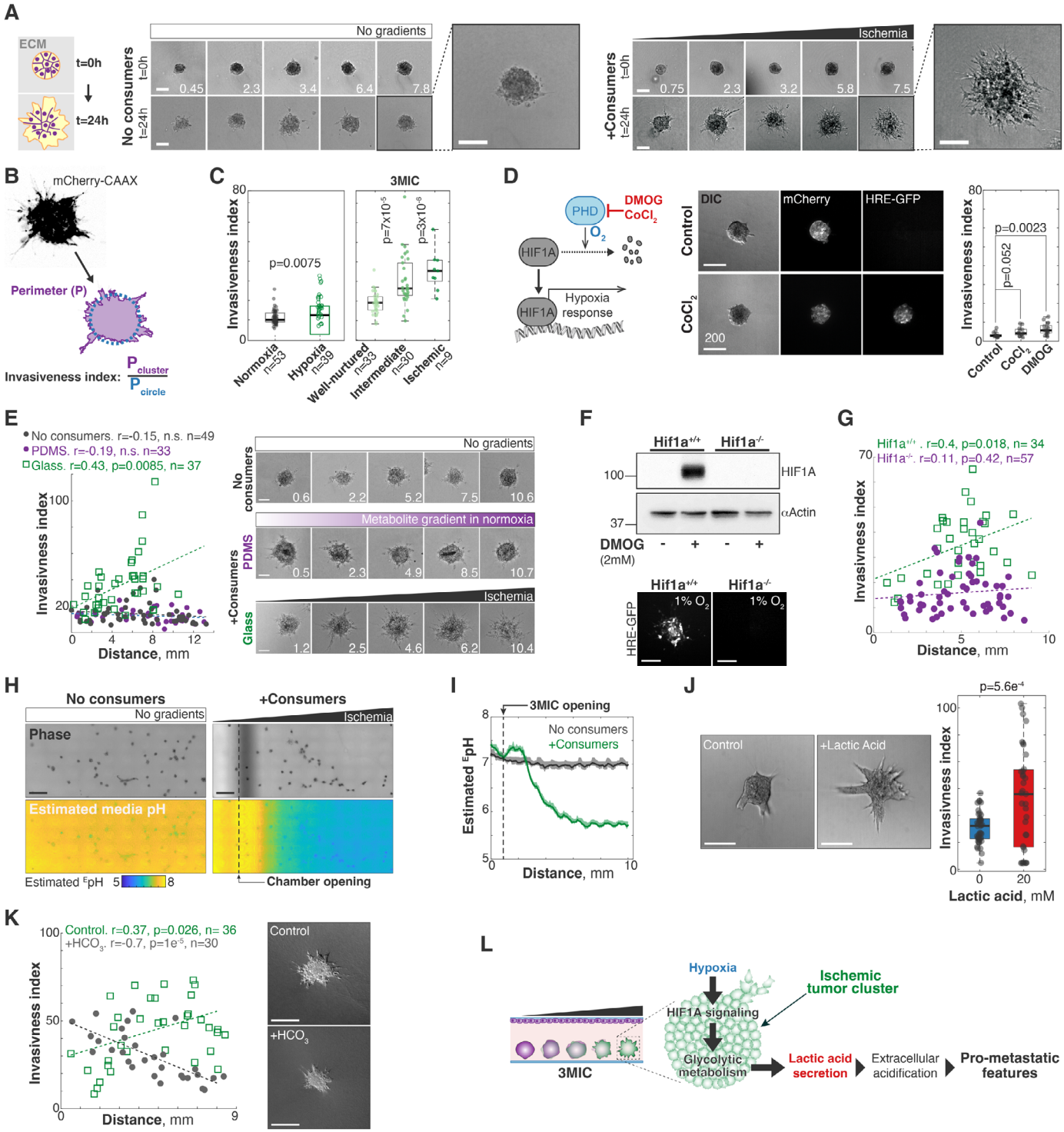

Figure 2: Low pH is responsible for the increased invasion of ischemic clusters in a HIF1A-dependent manner.

A. Left: Lung KP spheroids imaged after 0h (top) and 24h (bottom) of growth in different regions of the 3MIC without consumer cells. These clusters grew uniformly and retained smooth and round shapes.

Right: Similar data but for spheroids grown in the presence of consumer cells. Ischemic spheroids grew larger and more protrusive. Numbers in lower right corner denote the distance to the opening in mm. Bars: 100μm.

B. We defined invasiveness index, as the perimeter of tumor spheroid over the perimeter of a circle with the same area (1/circularity).

C. Using the invasiveness index, we quantified the invasiveness of lung KP spheroids under different environments. Well-nurtured, intermediate, and ischemic conditions correspond to different regions of the 3MIC. Data points: *per* spheroid invasiveness. Data from a representative example of two biological replicates.

D. Representative images and invasiveness index of untreated tumor spheroids compared to spheroids treated with $CoCl_2$ or DMOG. Bars: 200μm. See supplementary figure 2 for images of DMOG-treated spheroids.

E. Representative images of individual spheroids grown for 24h in the absence of consumer cells (top), or in the presence of consumer cells in 3MICs enclosed in PDMS (Polydimethylsiloxane) or glass (center and bottom, respectively). Numbers in lower right corner denote the distance to the chamber's opening in mm. Bars: 100μm. Plots on the right show a quantification of these changes. Data points: invasiveness index of individual spheroids. Dash lines: linear fit. Data from a representative experiment of two biological replicates.

F. Top: Anti-HIF1A blots of Hif1a$^{+/+}$ and Hif1a$^{-/-}$ cells treated or untreated with DMOG. Bottom: representative images of Hif1a$^{+/+}$ and Hif1a$^{-/-}$ HRE-GFP tumor spheroids cultured in a hypoxic incubator.

G. Quantification of the invasiveness index of Hif1a$^{+/+}$ and Hif1a$^{-/-}$ spheroids along the 3MIC. Bars: 200μm.

H. Representative ratiometric images used to estimate the extracellular pH (^{E}pH) within 3MICs with or without consumer cells.

I. Estimated extracellular pH over distance from the opening in 3MICs with or without consumer cells.

J. Representative images and quantification of the invasiveness index of lung KP spheroids treated with 20mM of lactic acid. Bars: 200μm.

K. Representative images and quantification of the invasiveness index of lung KP spheroids within 3MICs treated with 25mM of bicarbonate. Bars: 200μm.

L. Model suggested by our data where increased invasion under ischemia is driven by low extracellular pH through a HIF1A-dependent mechanism.

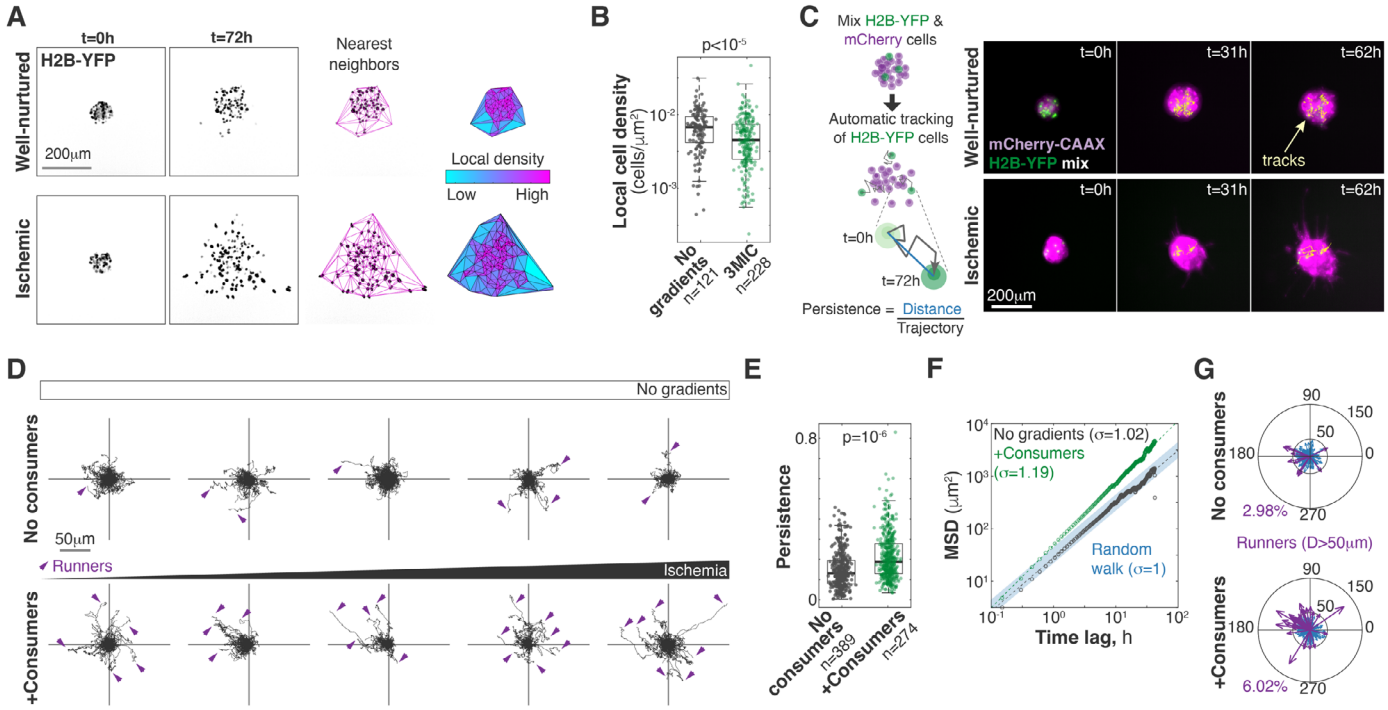

Figure 3: Ischemic cells in the 3MIC migrate more persistently

A. Image-based method to estimate local cell density. We located individual cells expressing the fluorescent nuclear marker H2B-YFP. We then triangulated closest neighbors and estimated areas between them. Local cell density corresponds to the inverse of each triangle's area.

B. Quantification of local cell densities over time for spheroids in the presence or absence of consumer cells. Data from 10 different spheroids (5 per condition).

C. Experimental setup and representative data of automatically tracked individual cells.

D. Top: migratory tracks of cells from 5 different tumor spheroids located at increasing distances from the opening of the 3MIC in the absence of consumer cells. Bottom: migratory tracks of cells from 5 different clusters located at similar distances from the opening as plots above but in the presence of consumer cells. Arrowheads show tracks for runner cells (defined as having a net displacement of 50μm or more).

E. Persistence of individual cells. Cells in ischemic spheroids are significantly more persistent than cells in well-nurtured spheroids. Data obtained from single cell tracks.

F. Mean-squared displacement (MSD) analysis of all tracked cells. Ischemic cells disperse more than what would be expected from a random walk (MSD constant α>1).

G. Compass plots showing the direction and magnitude of final displacement for individual cells. Runner cells are highlighted in purple. 3MIC opening (higher nutrients/oxygen levels) is to the left. Data from a representative experiment of three biological replicates.

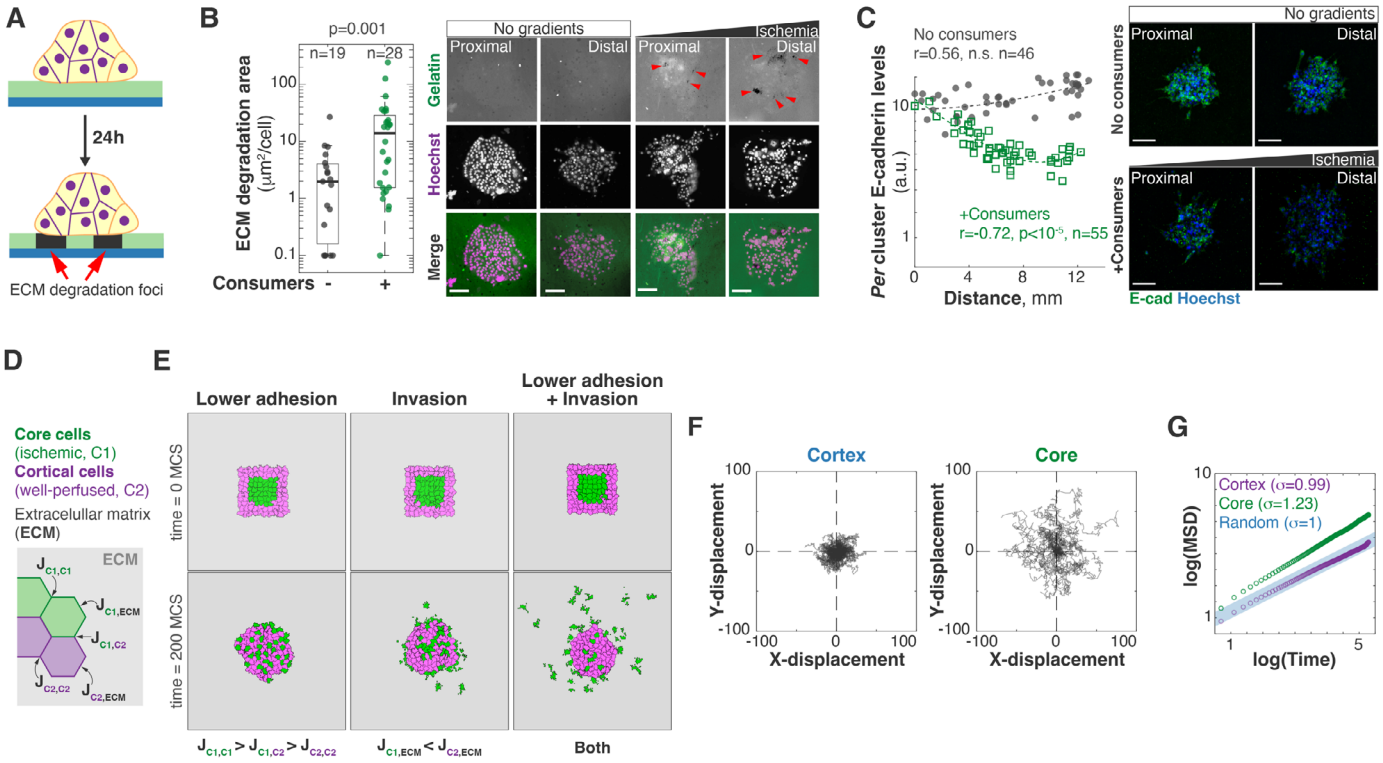

Figure 4: A decrease in epithelial adhesion and increased invasion can synergize to efficiently disperse tumor cells.

A. Schematic depicting the ECM degradation assay where spheroids are grown on a glass coated with fluorescent gelatin. Local loss of fluorescence indicates ECM degradation foci.

B. Representative images and quantification of ECM degradation. Spheroids were grown in the presence or absence of consumer cells. Ischemic spheroids show higher gelatin degradation (dark spots, red arrowheads). Bars: 100μm. Images compare spheroids located 2mm or closer to the opening of the 3MIC (Proximal) or further than 8mm (Distal). Data from a representative experiment of three biological replicates.

C. Representative images and quantification of Lung KP spheroids grown in the 3MIC and stained for E-cadherin (E-cad, green). Nuclei are stained with Hoechst (blue). Bars: 100μm. Images compare spheroids located 2mm or closer to the opening of the 3MIC (Proximal) or further than 8mm (Distal). Data points: *per* spheroid E-Cad levels. Dashed line: linear fit. Data from a representative experiment of three biological replicates.

D. Schematic depicting cell-cell and cell-substrate interaction energies from our Cellular Potts Model. See more details about the model on the main text and in the supplementary information.

E. Initial and final conditions of simulated tumor populations moving under different rules. The combination of lower epithelial adhesion and invasion, but not each process alone, efficiently increase the dispersion of ischemic (core) cells.

F. Tracks of simulated ischemic (core) and well-nurtured (cortical) cells modeled to have lower epithelial adhesion and increased invasion.

G. MSD of simulated well-nurtured and ischemic cells with lower epithelial adhesion and invasion. MSD changes are in the same order of magnitude as in our experimental data (Fig. 3F).

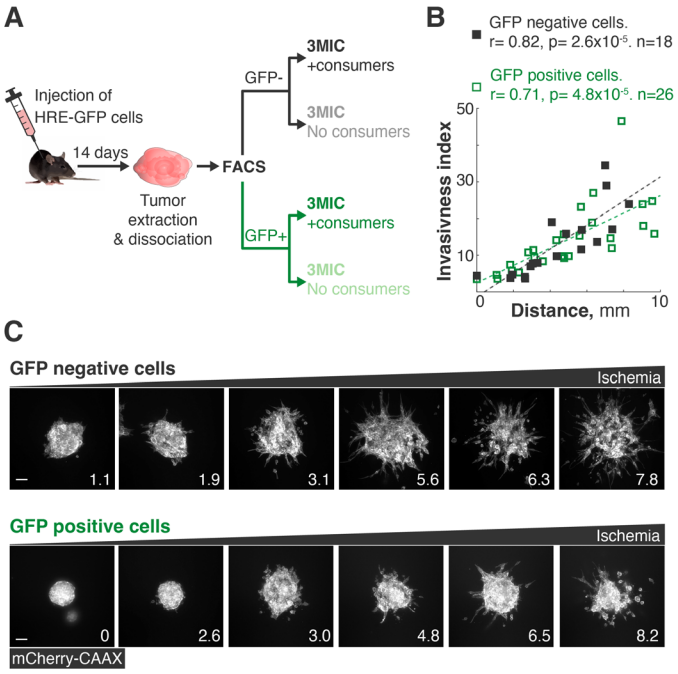

Figure 5: Tumor hypoxia *in vivo* did not induce permanent changes in the migratory potential of tumor cells.

A. Lung KP cells expressing HRE-GFP and mCherry-CAAX were injected subcutaneously in C57BL/6 mice and allowed to grow for 14 days. Tumors were then extracted and sorted into GFP positive (hypoxic/ischemic) and GFP negative (normoxic/well-nurtured) populations. These different sub-populations were grown as tumor spheroids in 3MICs in the absence or presence of consumer cells.
B. Quantification of invasiveness of experimental setup shown in (**A**). Data points: invasiveness index of individual spheroids. Dashed lines: linear fit. We observed similar invasion levels and response to ischemia in all spheroids regardless of if they were derived from well-nurtured or ischemic tumor regions.
C. Representative images of tumor spheroids derived from GFP positive and GFP negative cells growing at different locations inside of 3MICs. Numbers in lower right corner denote the distance to the opening in mm. Bars: 100μm.

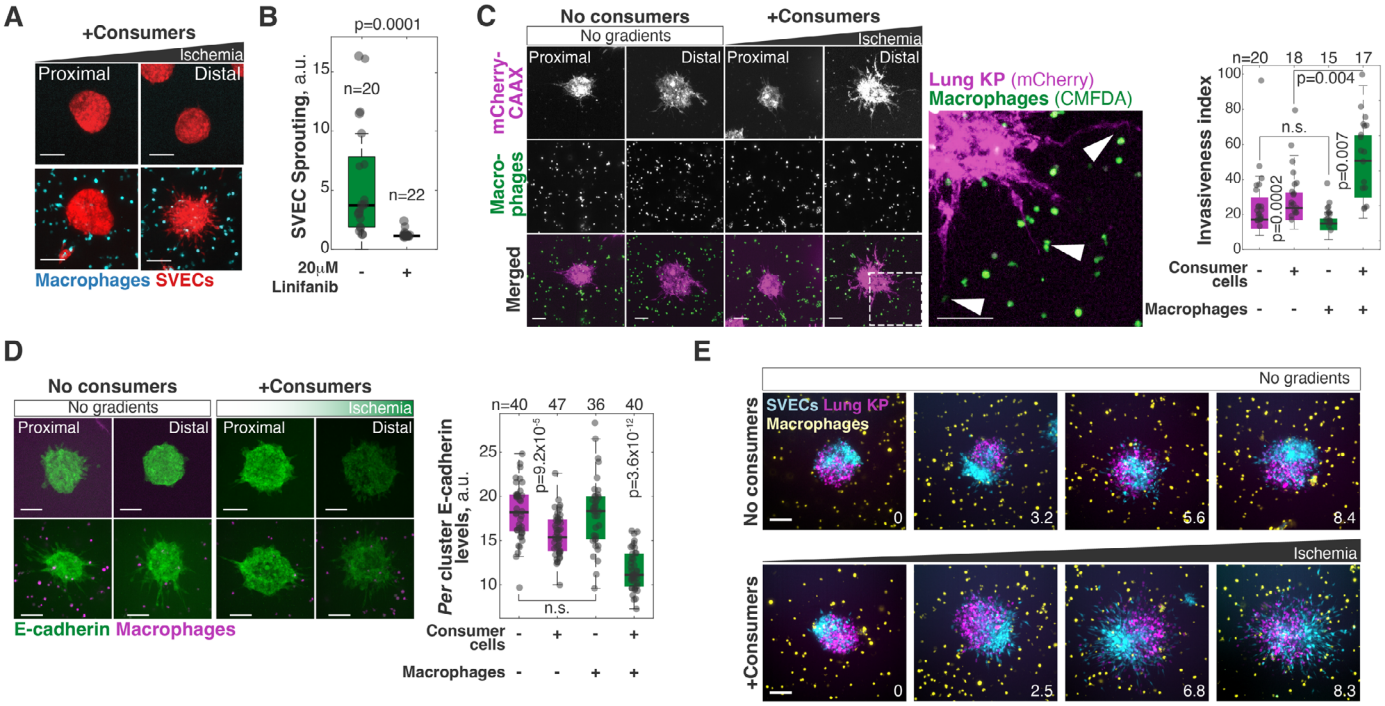

Figure 6: The 3MIC allowed the seamless implementation of cell co-cultures

A. Clusters of endothelial cells (SVECs, red) grown in 3MICs in the presence or absence of bone marrow-derived macrophages and stained with CMFDA (cyan). Bars: 100μm. Images compare spheroids located 2mm or closer to the opening of the 3MIC (Proximal) or further than 8mm (Distal). Data from a representative experiment of four biological replicates.

B. Quantification of SVEC sprouting in clusters co-cultured with macrophages. VEGFA inhibitor Linifanib abrogates sprouting induced by ischemic macrophages. Data from a representative experiment of two biological replicates.

C. Representative images and quantification of invasiveness of Lung KP spheroids co-cultured with BMDMs in the 3MIC. Ischemic macrophages significantly enhance tumor invasiveness and synergizes with ischemia. Region delineated with dashed lines is magnified on the right. Data points: *per* spheroid invasiveness. Bars: 100μm. Images compare spheroids located 2mm or closer to the opening of the 3MIC (Proximal) or further than 8mm (Distal). Data from a representative experiment of three biological replicates.

D. Representative images and quantification of Lung KP spheroids grown in the 3MIC and stained for E-cadherin (E-cad, green) in the presence or absence of macrophages (magenta). Ischemia and the presence of macrophages synergize in their reduction of E-Cad levels. Bars: 100 μm. Images compare spheroids located 2mm or closer to the opening of the 3MIC (Proximal) or further than 8mm (Distal). Data from a representative experiment of four biological replicates.

E. Representative images of triple co-cultures: chimeric Lung KP cells and SVEC spheroids, were grown in the presence of macrophages with or without consumer cells. Numbers in lower right corner denote the distance to the opening in mm. Bars: 100μm.

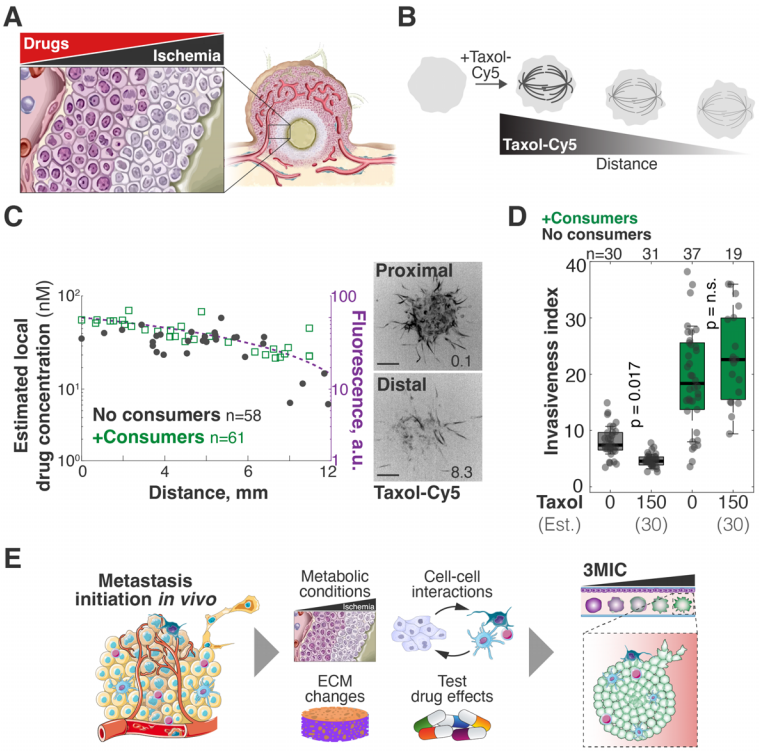

Figure 7: The 3MIC allows studying the effects of anti-migratory drugs on ischemic cells.
A. Cartoon showing that drug penetration of tumors is a therapeutic challenge, especially in ischemic regions where drug levels are likely lower.
B. Taxol-Cy5 is a probe used to fluorescently label microtubules. We used this property to estimate how Taxol levels decrease due to diffusion along the 3MIC.
C. Quantification of Taxol-Cy5 in spheroids within 3MICs with or without consumer cells. Plots indicate that drug levels decrease as they diffuse through 3MICs regardless of the presence of consumer cells or not. Dots: Taxol-Cy5 and location of single spheroids. Data pooled from two biological replicates.
D. Invasion of Taxol-treated spheroids growing in 3MICs with or without consumer cells. Cultures were treated with 150nM of Taxol which we estimated to drop to about 30nM deeper within 3MICs. Points: invasiveness of individual distal clusters (located at 4mm or more from the opening). Data from a representative experiment of three biological replicates.
E. Cartoon showing features of the 3MIC as an *ex vivo* model to study metastasis.

Supplementary Information

TABLE OF CONTENTS

Supplementary Figures 2
Supplementary Video Legends 12
Supplementary Tables..... 16

SUPPLEMENTARY FIGURES

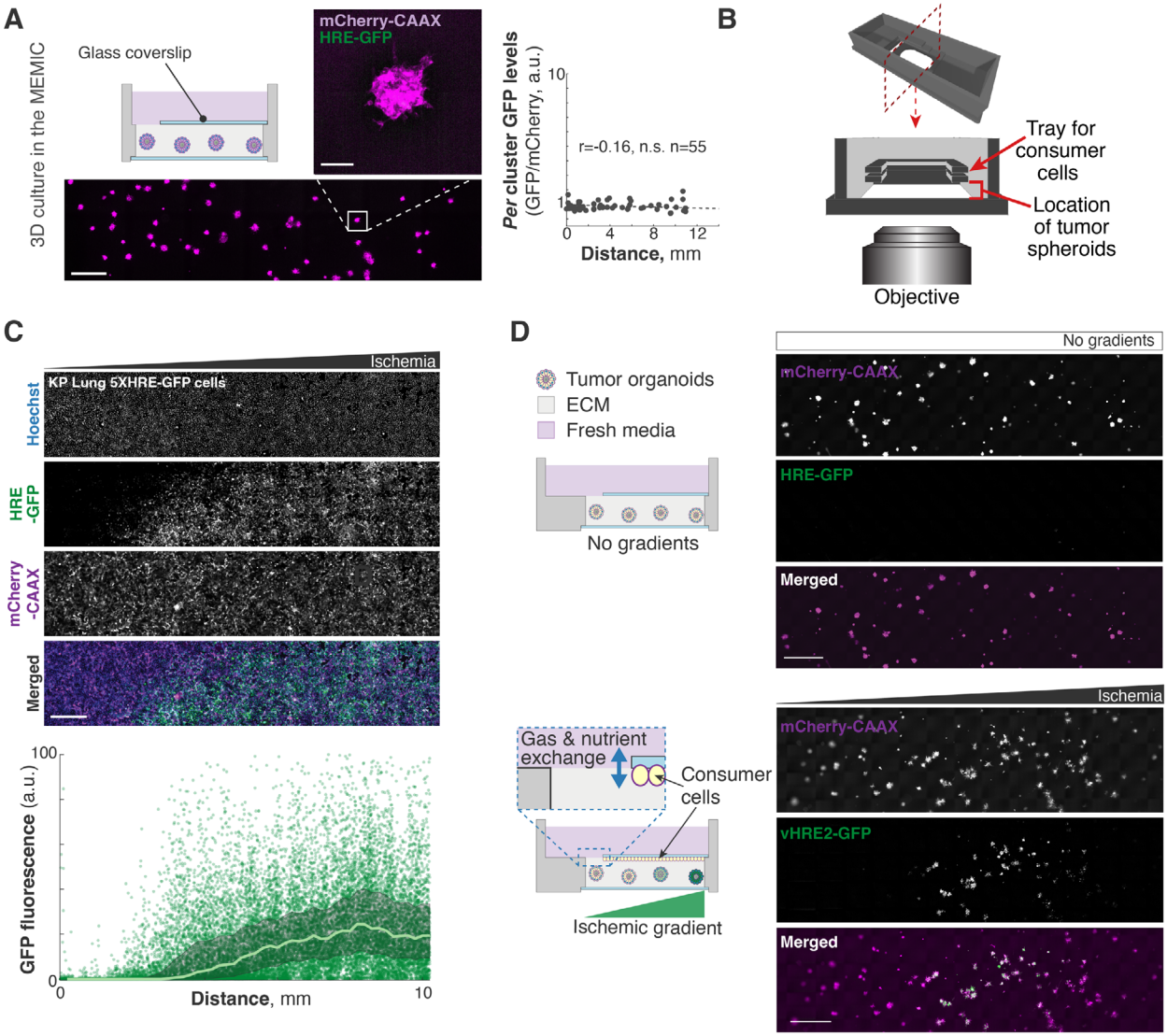

Supplementary Figure 1. Consumer cells are required to establish ischemic gradients within the 3MIC.

A. Spheroids grown in MEMICs fail to establish metabolic hypoxic gradients. Plot show the quantification of *per* spheroid GFP fluorescence (hypoxia reporter). Bars: 1000μm, and 100μm for insets.

B. Schematic showing the design of the 3MIC. A coverslip with attached consumer cells is slid into the holder above embedded clusters to create a nearly enclosed chamber. The rest of the structure contains fresh media.

C. Representative images of consumer cells expressing 5xHRE-GFP and mCherry-CAAX. Plot show the quantification of *per* spheroid GFP fluorescence (hypoxia reporter). Line: moving average. Bars: 1000μm

D. Spheroids of C6 glioma cells stably expressing a different hypoxia reporter (vHRE2-GFP[73]). Bars: 1000μm.

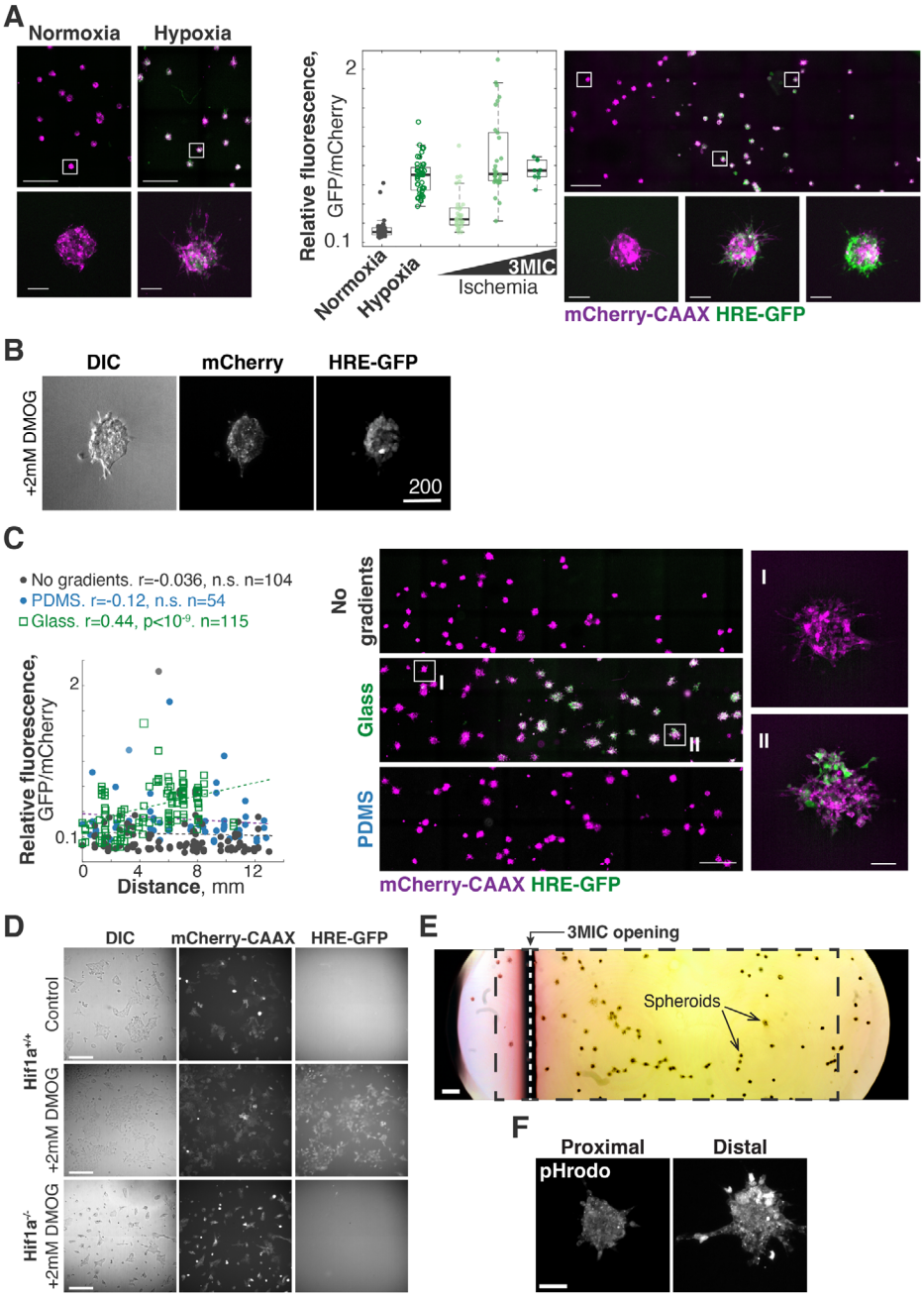

Supplementary Figure 2. HIF1A and acidification of the extracellular space are critical for the increased invasion in ischemic cells.

A. Lung KP spheroids were grown under normoxic, hypoxic and 3MIC conditions. Boxplots show GFP fluorescence (hypoxia) relative to mCherry-CAAX levels. Clusters in the 3MIC were grouped into three groups based on their distance from the opening. On the right, representative images of normoxic, hypoxic, and 3MIC conditions. Bars:1000μm,100μm for insets.

B. Representative images of tumor spheroids treated with DMOG. Bars: 200μm.

C. Lung KP spheroids expressing 5xHRE-GFP and mCherry-CAAX were grown without consumers, or in 3MICs enclosed in glass or PDMS. Points: *per* spheroid GFP (hypoxia) normalized to mCherry-CAAX

levels. Lines: linear fit. Panels on the show representative images of spheroids grown under no consumer, glass, and PDMS 3MICs. Bars: 1000μm, 100μm for insets.

D. 2D cultures of Hif1a$^{+/+}$ and Hif1a$^{-/-}$ cells treated or untreated with DMOG. These cells express HRE-GFP and mCherry-CAAX but as expected Hif1a$^{-/-}$ cells do not express GFP in response to DMOG. Bars: 100μm.

E. Color photo of a whole 3MIC with spheroids (see arrows) and consumer cells (not visible). Phenol red in the media shows a clear drop in extracellular pH. Black rectangle indicates the approximate area quantified in Fig. 2. Vertical white dashed line shows the opening of the 3MIC (shade below corresponds to the edge of the top coverslip). Bar: 500μm.

F. Tumor spheroids were cultured in the 3MIC and labelled with an intracellular pH fluorescent probe (pHrodo). We did not observe significant differences in fluorescence between well-nurtured and ischemic spheroids.

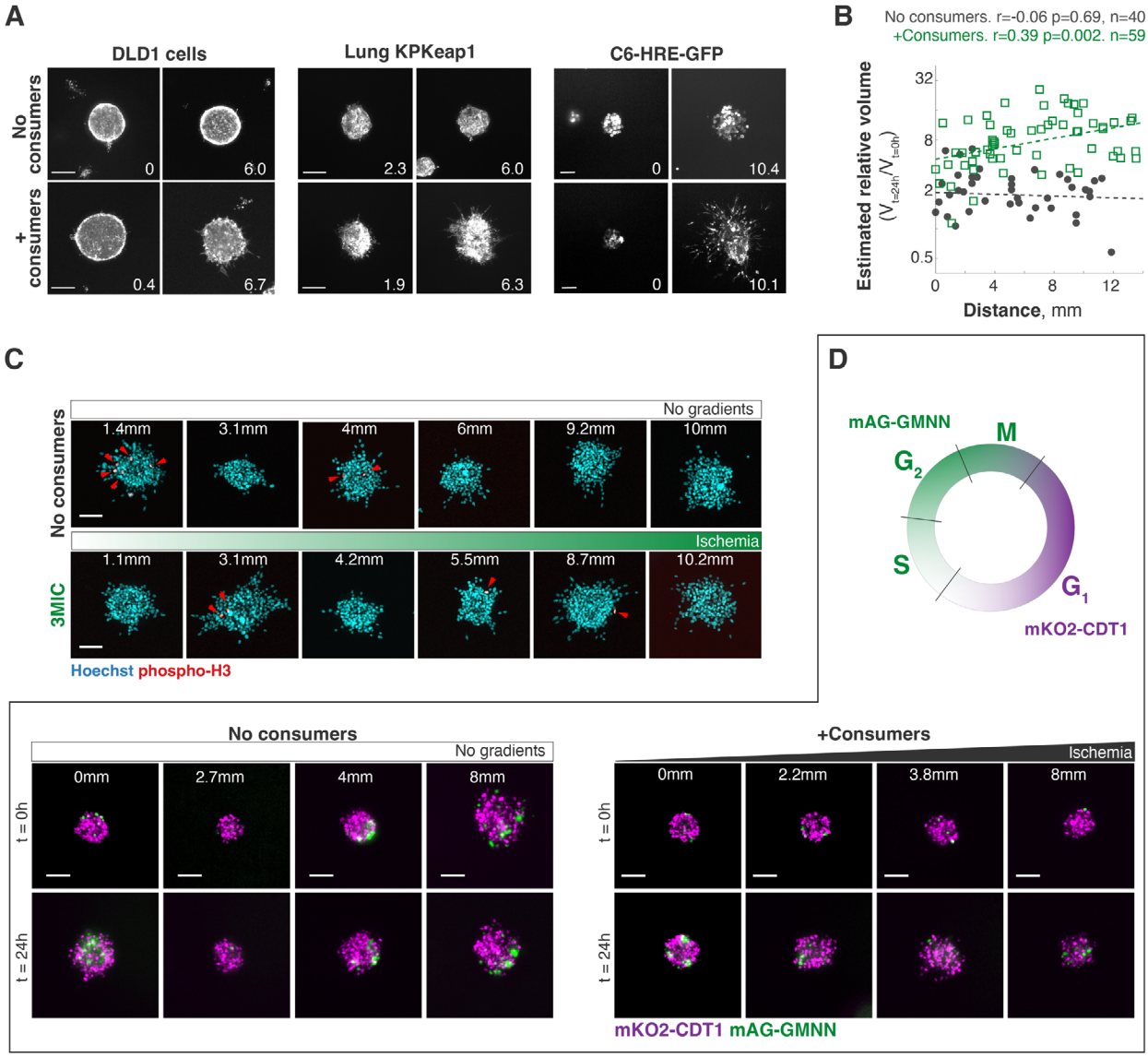
A
DLD1 cells
Lung KPKeap1
C6-HRE-GFP
No consumers
+ consumers
0
6.0
2.3
6.0
0
10.4
0.4
6.7
1.9
6.3
0
10.1
B
No consumers. r=-0.06 p=0.69, n=40
+Consumers. r=0.39 p=0.002. n=59
Estimated relative volume
(V t=24h/V t=0h)
32
8
2
0.5
0
4
8
12
Distance, mm
C
No gradients
No consumers
1.4mm
3.1mm
4mm
6mm
9.2mm
10mm
Ischemia
3MIC
1.1mm
3.1mm
4.2mm
5.5mm
8.7mm
10.2mm
Hoechst phospho-H3
D
mAG-GMNN
M
G2
S
G1
mKO2-CDT1
No consumers
No gradients
0mm
2.7mm
4mm
8mm
+Consumers
Ischemia
0mm
2.2mm
3.8mm
8mm
t = 0h
t = 24h
mKO2-CDT1 mAG-GMNN
E
Well-nurtured
100μm
Ischemic
0
Time (h)
72
F
No consumers
Runners
369 tracks
50μm
+Consumers
498 tracks
G
p=1e10-33
Speed (μm/sec)
0.2
0
H
p=0.033
Slope (σ)
1.4
1.2
1
0.8
No consumers
+ consumers
I
No consumers
No Gradients
p = 0.58
Y-displacement
80
0
-80
Runners
Weighted mean direction
-100
0
100
X-displacement
+Consumers
Ischemia
p = 0.07
Y-displacement
80
0
-80
-100
0
100
X-displacement
J
No consumers
+Consumers
p-values
10^0
10^-1
10^-2
p<0.05
10
30
50
Runner threshold

Supplementary Figure 3: Ischemia increases cell motility and invasion

A. Representative images of spheroids of DLD1 cells (colorectal adenocarcinoma cells), $KRAS^{G12D}$ p53-/- Keap1-/- cells (KPKeap1, lung adenocarcinoma) expressing 5xHRE-GFP and C6-hre-GFP cells (rat glioma) grown in 3MICs with or without consumers. Numbers in lower right corner denote the distance to the opening in mm. Bars: 100μm.

B. Quantification of estimated volume change of Lung KP spheroids. Points: area change of individual clusters, lines: linear fit.

C. Phospho-H3 immunofluorescence staining of Lung KP spheroids in 3MICs. Red arrows: proliferating cells. Bars: 100μm.

D. FUCCI-expressing lung KP clusters stably express mKO2-CDT1 in the G1 cell cycle phase or mAG-GMNN in other phases of the cell cycle. Clusters growing in the absence of ischemic gradients have many proliferating cells throughout the duration of the experiment, whereas ischemic clusters in the 3MIC have progressively lower numbers of proliferating cells, showing a higher portion of cells in G1. Bars: 100μm.

E. Temporal projection of a representative ischemic cluster over a 72h time-lapse.

F. Migratory tracks for all cells tracked in 3MICs and pooled according to the presence or absence of consumers. Tracks of cells that with a net displacement of 50μm or more (runners) are highlighted in magenta.

G. Top: Instantaneous speeds of individual cells in the presence or absence of consumers. Bottom: MSD constants for cells moving in the presence or absence of consumers. Each dote is the MSD constant calculated from multiple tracks within one spheroid.

H. Final position of each tracked cell centered to their origins. Magenta vectors highlight the displacement and direction of runner cells. Vector sum (orange) shows a small bias towards higher nutrient levels in the presence of consumers. However, this bias is only significant (Raleigh-Moore directional test) under some thresholds to define 'runner cells' (**I**).

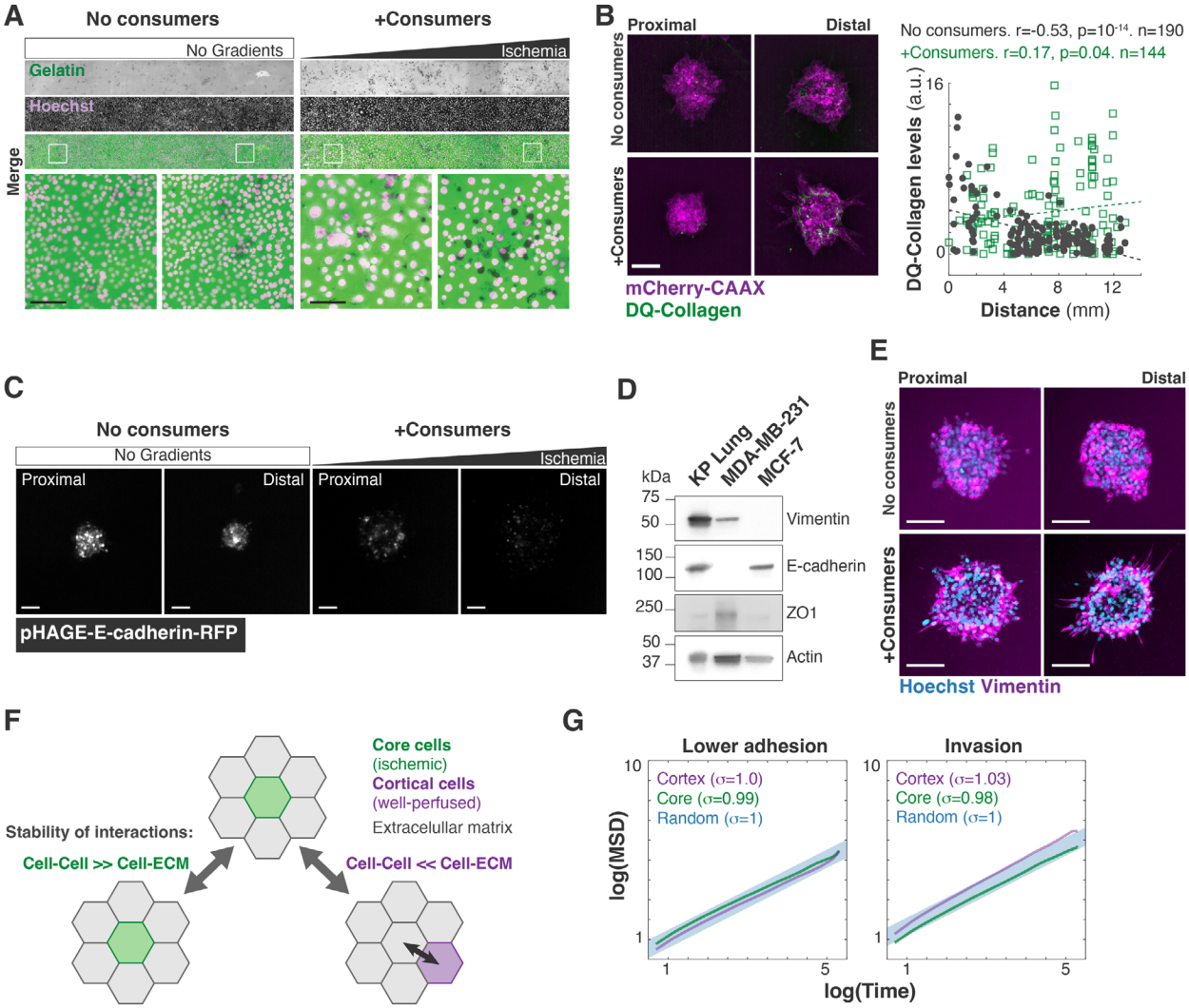

Supplementary Figure 4: Ischemia enhances invasiveness of Lung KP spheroids.

A. Lung KP cells were grown on 488-Gelatin coated coverslips and used as consumers. Increase in degradation of gelatin was observed with increase in distance from the opening in 3MIC, while no significant degradation was observed under no gradient conditions. Bars: 100μm.

B. Right: representative images of Lung KP spheroids grown on DQ collagen. The distal ischemic spheroids increased their collagen/ECM cleavage. Bars: 100μm. Left: quantification of fluorescence intensity of DQ collagen showing a gradual increase in cleaved collagen with increase in distance of the spheroid from the opening. Points: DQ-collagen levels per cluster (GFP-fluorescence intensity normalized to mCherry-CAAX fluorescence). Dashed line: linear fit

C. Lung KP tumor spheroids stably expressing pHAGE-E-cadherin-RFP (E-cadherin reporter). Bars: 100μm.

D. Western blot analysis of EMT markers in Lung KP cells.

E. Representative images of Lung KP spheroids grown in the 3MIC and stained for vimentin. Bars: 100μm.

F. In the Cellular Potts model illustrating our model of ECM invasion. This model is mechanistically agnostic. It only says that in ischemic cells, the affinity to the ECM relative to cells in higher than in well nurtured cells. This simple rule increases the chance of a localization “swap” of ischemic cells into the ECM.

G. Mean-squared displacement analysis for simulated well-nurtured cells and ischemic cells. Models included lower cell-cell adhesion in ischemia or increased invasion. The synergistic effects of both properties are shown in main figure 4.

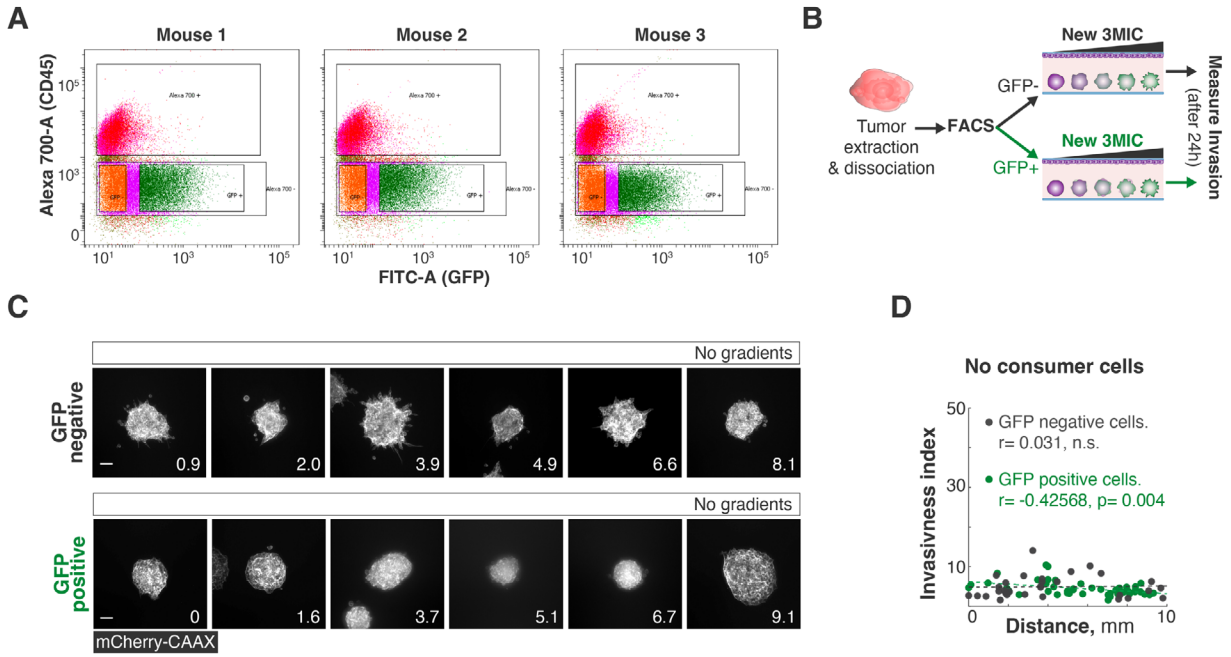

Supplementary Figure 5: Ischemia-induced changes are phenotypic.
A. $3x10^5$ Lung KP cells expressing 5xHRE-GFP were injected subcutaneously into the flank of syngenetic mice. Tumors were then dissociated into single cells which were then FACS-separated into GFP+ and GFP- populations. Plots show FACS data for tumor from three different mice.
B. Experimental workflow: sorted cells were then grown in separate 3MICs with or without consumers.
C. Representative images of spheroids culture in 3MICs with no gradients (no consumers). Bars: 100μm.
D. In the absence of consumers, cells derived from hypoxic tumor regions did not show a significant increase of invasion or motility.

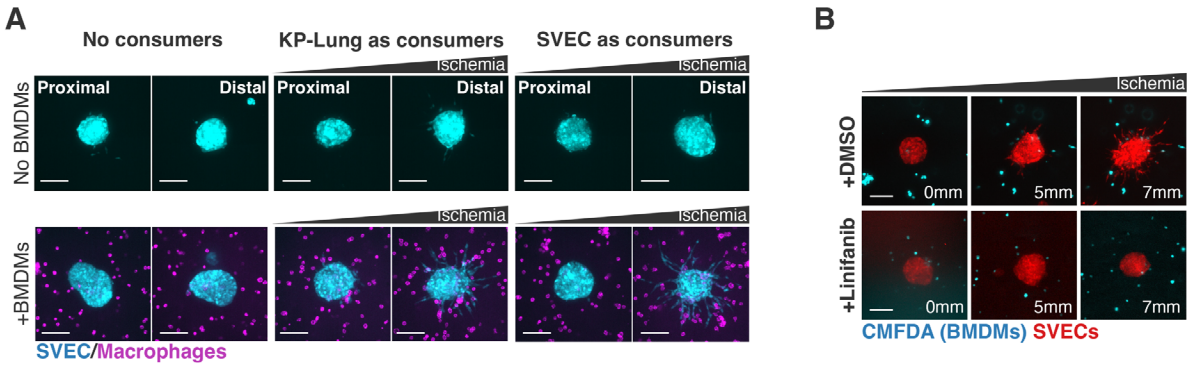

Supplementary Figure 6: Ischemic macrophages induce sprouting of SVEC spheroids.
A. Representative images of SVEC clusters co-cultured with macrophages in the absence of (no gradients) or presence of different cell types as consumers. Bars: 100μm. We did not observe a major effect of the consumer cell types but none replaced the pro-sprouting effects of macrophages. Images compare spheroids located 2mm or closer to the opening of the 3MIC (Proximal) or further than 8mm (Distal).
B. In the presence of consumers (in this case also SVECs), BMDMs dramatically increase sprouting in SVEC clusters. This effect is abrogated by the VEGFA inhibitor Linifanib. Bars: 100μm.

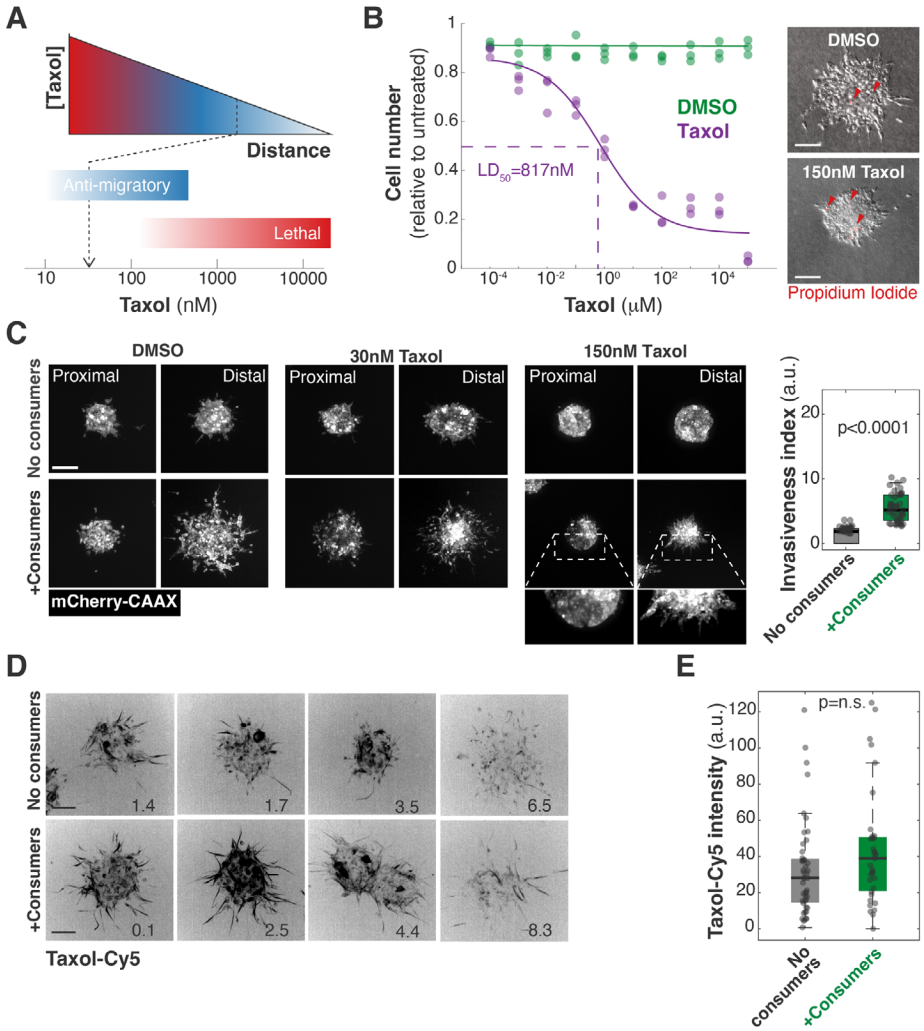

Supplementary Figure 7: Ischemic spheroids are resistant to the anti-motility effects of Taxol.
A. Schematic representation of lethal and sub-lethal as Taxol levels decrease with the distance to its source. We asked here is we can determine Taxol levels within 3MICs and test if those values have the same effects on ischemic cells and well-nurtured cells. We found that while about 30nM of Taxol inhibit the movements of well-nurtured cells, ischemic cells were not sensitive to these Taxol levels.
B. Lung KP cells were treated with different doses of Taxol for 24 hours. Viability was determined by propidium iodide (PI) incorporation to determine the IC_{50} values. Representative images on the right illustrate that spheroids showed no significant differences in cell viability when spheroids were treated with doses of 150nM Taxol or lower. Arrowheads: Propidium positive non-viable cells.
C. Representative images and quantification of Lung KP spheroids treated and untreated with 150nM Taxol. Distal spheroids can invade the ECM even when treated with Taxol but only in the presence of consumers (ischemia). Bars: 100μm.
D. Representative images of Lung KP clusters grown in the 3MIC in the presence or absence of gradients and treated with a fluorescent Taxol analog (Taxol-Cy5). We used its fluorescent signal to estimate local levels of the drug in the 3MIC. Numbers in lower right corner denote the distance to the opening in mm. Bars: 100μm.
E. Boxplot showing Taxol-Cy5 levels in spheroids within 3MICs with or without consumer cells. Dots: *per* spheroid Taxol-Cy5 levels.

SUPPLEMENTARY VIDEO LEGENDS

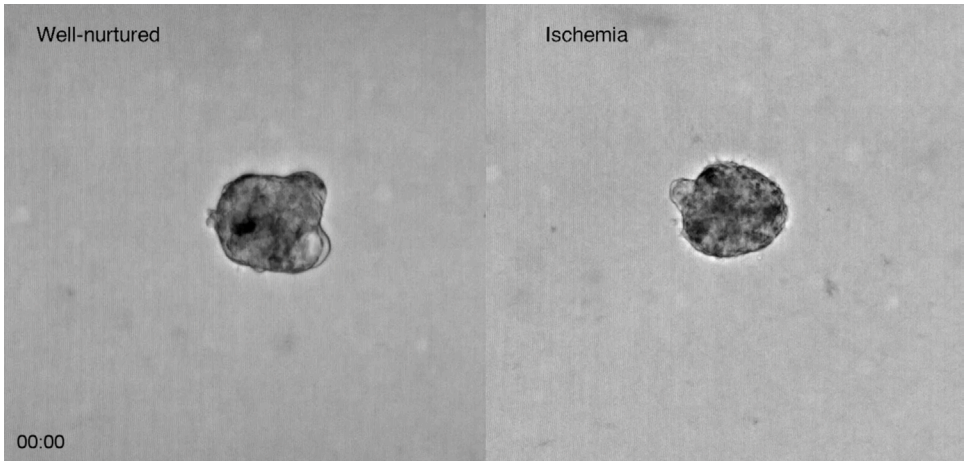

Video S1. Lung KP spheroids grown in 3MIC. Left panel shows spheroid growing close to the opening of 3MIC (well-nourished) and right panel shows a spheroid growing in the ischemic region of 3MIC. Images were acquired every 15 mins for a period of 72 hours.

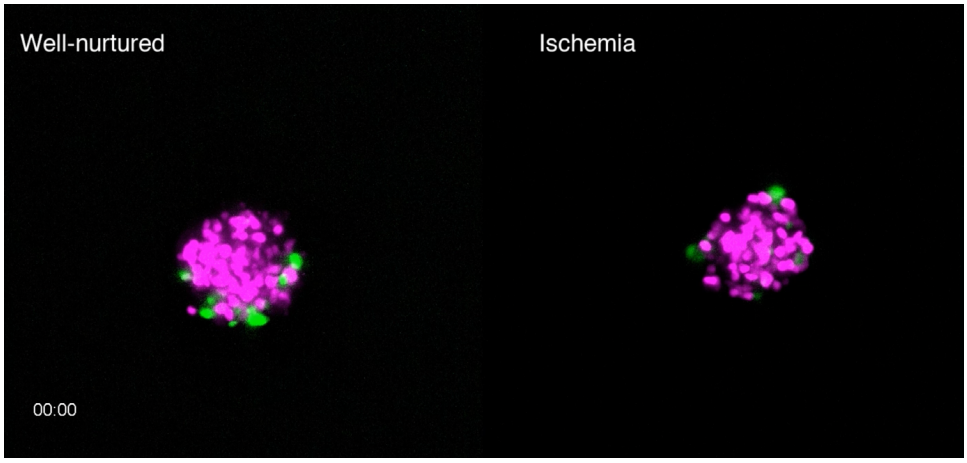

Video S2. Lung KP spheroids stably expressing the pBOB-EF1-FastFUCCI-Puro construct were grown in 3MIC. Movie shows the cell-cycle progression of the cells in the spheroids growing in well-nourished regions (left panel) and ischemic regions (right panel).

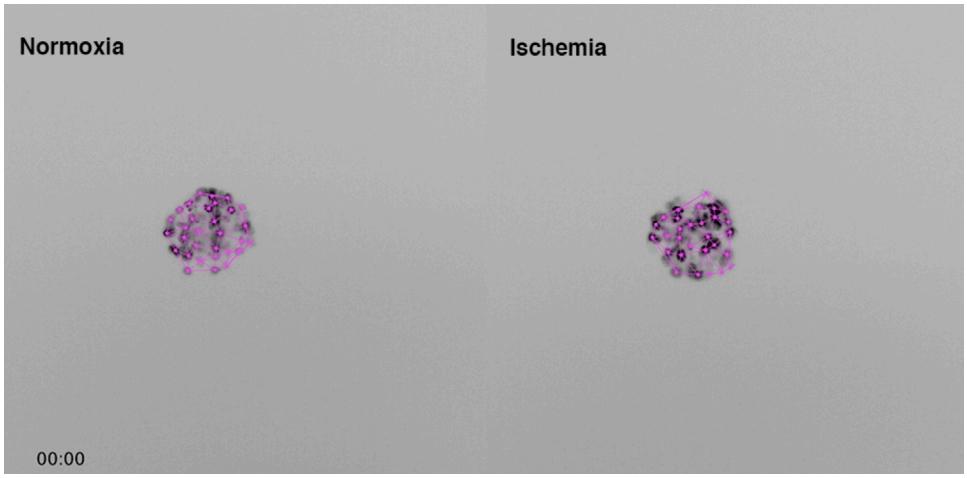

Video S3. Movie depicting the decrease in cell density (or increase of area in between cells). Cells are labelled with H2B-YFP (black). Purple lines show results from Delaunay triangulation algorithm.

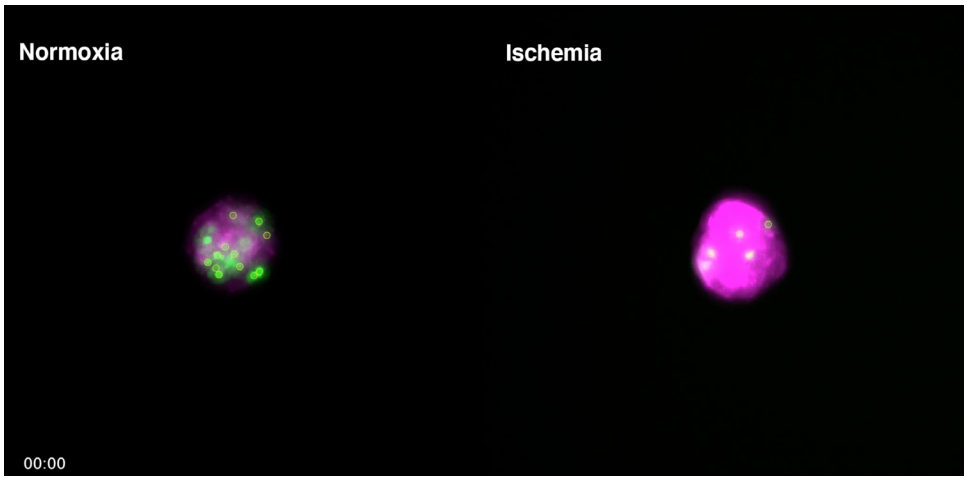

Video S4. Chimeric Lung KP spheroids of cells expressing H2B-YFP (green) or mCherry-CAAX (magenta) mixed at a 1:4 ratio. Time-lapse video shows the migration tracks of H2B-YFP positive cells in spheroids grown in well-nurtured and ischemic regions of 3MIC.

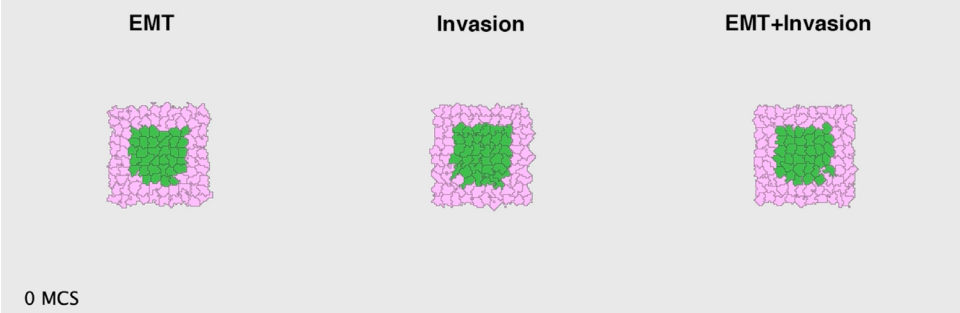

Video S5. Movie depicting the evolution of three Cellular Potts Models simulating the movements of cells arranged as a core of 'ischemic' cells surrounded by cortical, well-nurtured cells. In these models, core cells are assigned a reduced epithelial cell adhesion, increased ECM invasion, or the combination of both using. MCS: Monte Carlo Step (time unit).

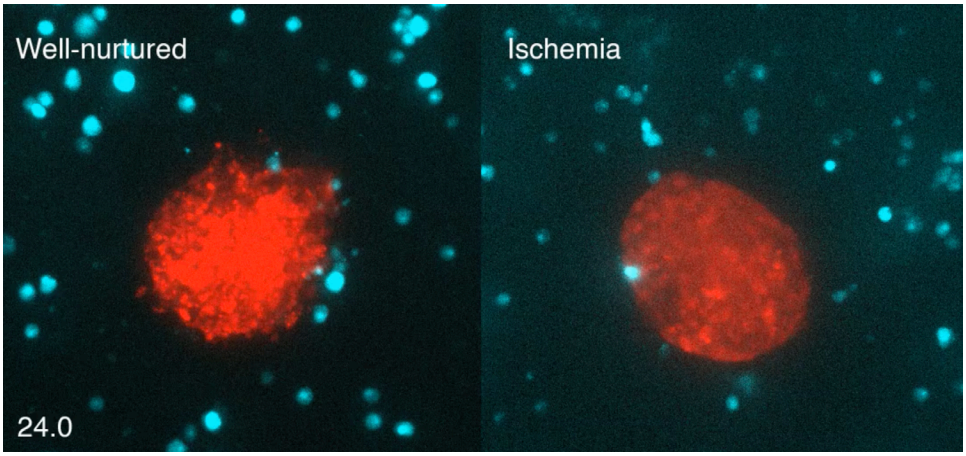

Video S6. Time lapse of SVEC spheroids (expressing mCherry, red), growing in the 3MIC with BMDMs (labelled with CMFDA, cyan) embedded in the ECM. Images were acquired from 24 hours every 30 mins for a period of 72 hours.

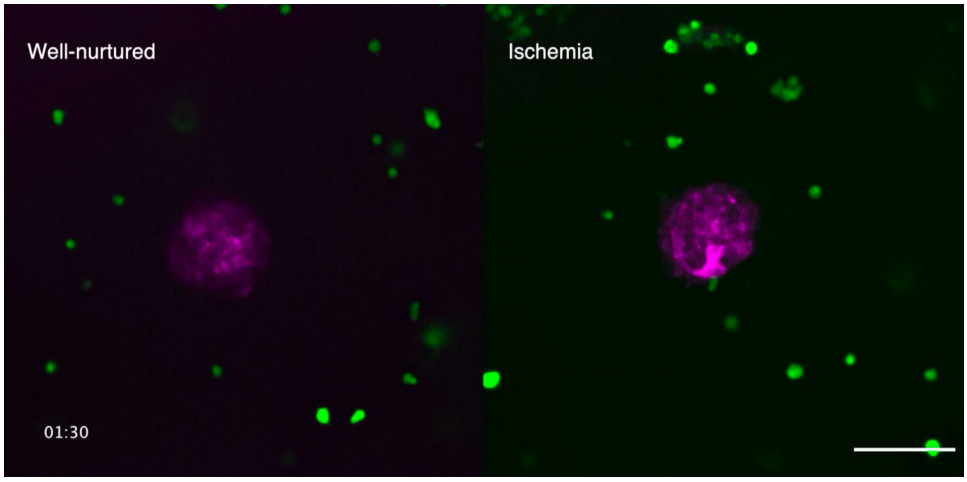

Video S7. Time lapse of Lung KP (expressing mCherry-CAAX, magenta) spheroids growing in 3MIC in the 3MIC with BMDMs (labelled with CMFDA, green) embedded in the ECM. Images were acquired every 30 mins for a period of 72 hours.

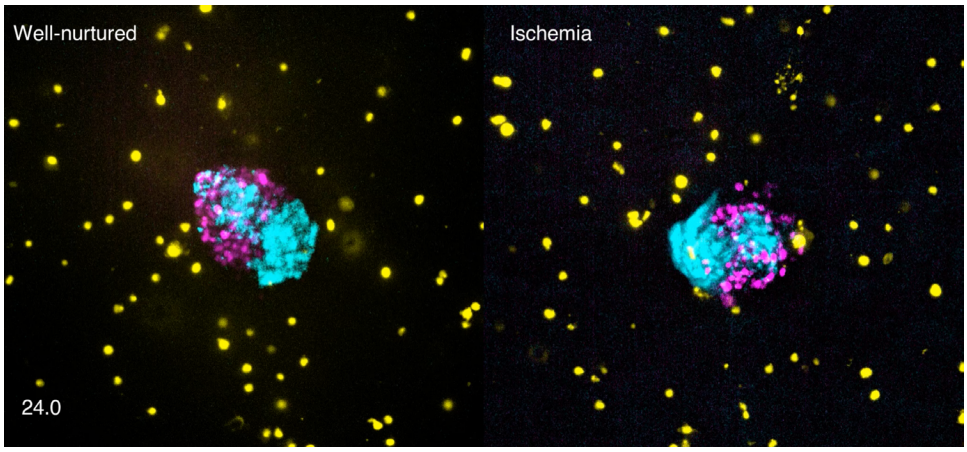

Video S8. Time lapse of spheroids formed by Lung KP cells (magenta) and SVECs (cyan), growing in the 3MIC with BMDMs (yellow) embedded in the ECM. Images were acquired from 24 hours every 30 mins for a period of 66 hours.

SUPPLEMENTARY TABLES

Condition	$J_{C1,C1}$	$J_{C1,C2}$	$J_{C2,C2}$	$J_{C1,ECM}$	$J_{C2,ECM}$
Increased Invasion	16	16	16	2	11
Decreased epithelial adhesion	24	16	8	11	11
Both	24	16	8	2	11

Table S1. CPM parameters for different conditions. $J_{C1,C1}$ is the surface energy between to cells or a cell and the ECM. Higher surface energies lead to lower affinity. C1: core cells. C2: cortical cells. ECM: Substrate (extracellular matrix).

Parameter	Value	Units
Temperature	37	ºC
Population size	100	cells
Target cell size	40	pixels
Dimensions	200x200	pixels
Boundary conditions	Periodic	N/A

Table S2. Additional CPM parameters.